© 2026. Published by The Company of Biologists | Development (2026) 153, dev205775. doi:10.1242/dev.205775

RESEARCH ARTICLE

HUMAN DEVELOPMENT

Notch signalling governs human enteric nervous system progenitor dynamics

Antigoni Gogolou[1,2], Nikolas Stefanidis[1,3], Fay Cooper[1,2], Guillaume Blin[4,5], Stanley E. Strawbridge[1,6,7], Alexander G. Fletcher[2,3,7] and Anestis Tsakiridis[1,2,*]

ABSTRACT

The enteric nervous system (ENS) is the main branch of the peripheral nervous system that innervates the gastrointestinal tract controlling vital functions. It arises during embryogenesis via migration, proliferation and differentiation of neural crest-derived ENS progenitors. Perturbation of these processes, caused by mutations in key signalling pathway components and transcription factors, prevents progenitor colonisation of the distal gut, causing aganglionic phenotypes and enteric neuropathies such as Hirschsprung (HSCR) disease. While animal models implicate Notch signalling in ENS specification, its role in human ENS progenitor cell fate decisions remains unclear. Here, we employ a human pluripotent stem cell-based model to show that Notch signalling is a key regulator of human ENS progenitor dynamics. Quantitative modelling of our *in vitro* data indicates that Notch inhibition accelerates progenitor differentiation without substantially altering neuronal versus glial lineage bias. Furthermore, we establish that Notch signalling controls human ENS progenitor migration by influencing migration velocity and directionality. Together, these findings provide mechanistic insights into how Notch signalling disruption may contribute to the pathogenesis of human intestinal aganglionosis.

KEY WORDS: Enteric nervous system, Human pluripotent stem cells, Notch, Differentiation, Hirschsprung disease

INTRODUCTION

The gastrointestinal tract is primarily innervated by the intrinsic enteric nervous system (ENS), a complex network of neurons and glia organised into ganglia. The ENS controls several essential gut functions, including bowel motility, nutrient absorption and digestion, secretion of water, electrolytes and hormones, and blood flow (Kang et al., 2021). It arises during embryonic development predominantly from the vagal neural crest (NC), a multipotent cell population specified at the neural plate border between somites 1 and 7 (Le Douarin and Teillet, 1973; Yntema and Hammond, 1954). After delaminating from the dorsal neural tube, vagal NC cells migrate into the foregut, while acquiring neuroglial-potent ENS progenitor features, and colonise the developing gut in a rostro-caudal direction.

The generation of appropriate proportions of enteric neurons and glia across space and time depends on the coordinated regulation of ENS progenitor migration, proliferation and differentiation. Recent single-cell RNA-sequencing analysis in the mouse has challenged the long-held view that ENS progenitors remain uniformly bipotent throughout development, with equal propensity to generate enteric neurons and glia (Laddach et al., 2023). Instead, this study supports a model in which ENS progenitors are initially biased toward neurogenic differentiation and subsequently progress toward a default, quiescent gliogenic state. This branching of neurogenic differentiation trajectories from a linear gliogenic axis coincides with a progressive decline in progenitor proliferative capacity, and in migratory and colonisation potential (Zhang et al., 2019). Whether human ENS progenitors exhibit similar developmental dynamics remains unclear.

Disruption of ENS progenitor dynamics, caused by mutations in key signalling pathway components (e.g. *RET* and *EDNRB*) and transcription factors (e.g. *SOX10*), leads to failure of ENS progenitors to colonise the distal gut and, consequently, to aganglionic phenotypes and enteric neuropathies (Kang et al., 2021; Heuckeroth, 2018). Hirschsprung disease (HSCR) is the most representative of these conditions, and is caused by the absence of enteric neurons in the distal bowel, which consequently loses propulsive motility, ultimately resulting in lethal intestinal obstruction (Heuckeroth, 2018). Thus, understanding how human ENS progenitor ontogeny is orchestrated at the molecular and cellular levels is crucial for improving insight into the causes of enteric neuropathies.

One signalling pathway implicated in ENS development is Notch, a well-established and evolutionarily conserved modulator of cell fate. Notch receptors and their ligands, Delta and Jagged (in mammals), are transmembrane proteins that typically mediate interactions between adjacent cells. Ligand-receptor binding triggers a series of proteolytic events that ultimately lead to γ-secretase-dependent release of the Notch intracellular domain (NICD) from the cell membrane. NICD then translocates to the nucleus, where it cooperates with transcriptional effectors such as CBF1/RBP-Jκ to induce transcription of target genes, including the basic helix–loop–helix hairy and enhancer of split (HES) proteins (Bray, 2016).

In animal models, Notch signalling components are dynamically expressed in ENS progenitors, their derivatives and the surrounding

[1]Centre for Stem Cell Biology, School of Biosciences, The University of Sheffield, Sheffield S10 2TN, UK. [2]Neuroscience Institute, The University of Sheffield, Sheffield S10 2TN, UK. [3]School of Mathematical and Physical Sciences, University of Sheffield, Hicks Building, Hounsfield Road, Sheffield S3 7RH, UK. [4]Institute for Stem Cell Research, School of Biological Sciences, The University of Edinburgh, Edinburgh EH16 4UU, UK. [5]Centre for Regenerative Medicine, Institute for Regeneration and Repair, The University of Edinburgh, Edinburgh EH16 4UU, UK. [6]Bateson Centre for Disease Mechanisms, University of Sheffield, Sheffield, UK. [7]Insigneo Institute, University of Sheffield, Sheffield S10 2TA, UK.

*Author for correspondence (a.tsakiridis@sheffield.ac.uk)

A.G., 0000-0002-3581-2426; N.S., 0009-0009-7311-4977; F.C., 0000-0002-5340-619X; G.B., 0000-0002-9295-237X; S.E.S., 0000-0003-0273-0835; A.G.F., 0000-0003-0525-4336; A.T., 0000-0002-2184-2990

This is an Open Access article distributed under the terms of the Creative Commons Attribution License (https://creativecommons.org/licenses/by/4.0), which permits unrestricted use, distribution and reproduction in any medium provided that the original work is properly attributed.

Handling Editor: James Wells
Received 30 April 2026; Accepted 21 September 2026

Development (2026) 153, dev205775. doi:10.1242/dev.205775

intestinal mesenchyme (Laddach et al., 2023; Sander et al., 2003; Liu and Ngan, 2014; Zhou et al., 2024; Jacobs-Li et al., 2023; Kuil et al., 2023; Morarach et al., 2021; McCallum et al., 2020). Moreover, deletion of Notch pathway members in mouse embryos disrupts multiple aspects of ENS development, including ENS progenitor maintenance, migration, proliferation and differentiation (Mead and Yutzey, 2012; Okamura and Saga, 2008; Taylor et al., 2007; de Bellard et al., 2002). In line with these findings, expression of Notch pathway components is significantly perturbed in both animal and induced pluripotent stem cell (iPSC)-based models of HSCR, as well as in patient tissues (Vincent et al., 2023; Li et al., 2023; Ngan et al., 2011; Windster et al., 2025; Jia et al., 2012). Furthermore, genetic variant screening and genome-wide association studies have identified links between Notch-related mutations and HSCR (Ngan et al., 2011; Tang et al., 2017). However, the behaviour of human ENS progenitor cells under steady-state and disrupted Notch signalling conditions has not been comprehensively investigated.

We have previously established a protocol for the efficient generation of vagal NC cells exhibiting features of early ENS progenitors from human pluripotent stem cells (hPSCs) (Jevans et al., 2024; Gogolou et al., 2021; Frith et al., 2020). These cells were shown to efficiently colonise the ENS of immunocompromised mice, giving rise to neuronal and glial lineages following *in vivo* transplantation (Frith et al., 2020), and to improve contractility in aganglionic gut explants obtained from individuals with HSCR (Jevans et al., 2024). Here, we provide a detailed characterisation of the stepwise transition of these hPSC-derived vagal NC cells into later-stage ENS progenitors, enteric neurons and glia *in vitro*, thereby establishing a robust model of human ENS development. Using this platform, we show that Notch signalling components are dynamically expressed during human ENS specification. Chemically inhibiting Notch signalling dramatically enhances the production of enteric neurons and glia. Computational modelling of our data, combined with compositional likelihood-based parameter inference and model selection, supports a branching differentiation hierarchy marked by an early pro-neurogenic bias. Our modelling further reveals that Notch inhibition alters developmental tempo, accelerating ENS progenitor differentiation and triggering the premature production of both neurons and glia. This effect is accompanied by increased neuronal clustering and reduced migratory capacity of ENS progenitors.

Together, our findings strongly support a crucial role for Notch signalling in regulating the differentiation pace of human ENS progenitors. We propose that disruption in the temporal production of their neuronal and glial derivatives, coupled with impaired colonization potential, may underlie Notch-associated aganglionic phenotypes.

RESULTS

Characterisation of an *in vitro* model of human ENS development

We have previously defined culture conditions for the directed differentiation of hPSCs toward vagal NC cells and ENS cells (Frith et al., 2020; Gogolou et al., 2021). Our protocol involves the initial generation of an anterior NC progenitor population by day 4 of differentiation (D4) through combined stimulation of WNT signalling (via treatment with the GSK3 inhibitor CHIR99021), inhibition of TGFβ signalling and moderate BMP activity. This is followed by the addition of retinoic acid (RA) to induce cells with vagal NC/early ENS progenitor features at D6 (Fig. 1A). D6 vagal NC/ENS progenitor cultures are then dissociated and cultured as non-adherent spheres in the presence of WNT, FGF and RA signalling agonists for a further 3 days. The spheres are subsequently plated and cultured in neurogenic conditions to promote subsequent differentiation toward ENS components (Fig. 1A).

We sought to characterize in detail the later stages of the protocol, after vagal NC specification, following sphere attachment and the differentiation of vagal NC-derived ENS progenitors into their derivatives. To this end, we differentiated hPSCs (the well-established iPSC line WTC11; Miyaoka et al., 2014) according to our protocol up to D50 (Fig. 1A). Time-course quantitative PCR (qPCR) analysis revealed that, following maximal induction at D6 (vagal NC stage), expression of the NC/ENS progenitor/glial marker *SOX10* progressively declined with differentiation time. In contrast, levels of the committed ENS progenitor/pro-neural regulators *ASCL1*, *PHOX2B* and *RET* (Taraviras et al., 1999; Pattyn et al., 1999; Young et al., 2003; Memic et al., 2016) remained stable or increased between D22 and D50 (Fig. 1B). From D22 onwards, we detected induction of transcripts characteristic of enteric neurons [*TRKC* (*NTRK3*), *PRPH* and *TH*] (Chalazonitis et al., 2001; Morarach et al., 2021; Jacobs-Li et al., 2023; Szabolcs et al., 1996; Recinto et al., 2024), including markers of specific neuronal subtypes such as *SST* (interneurons) (Morarach et al., 2021), *HTR2A* (serotonergic neurons) (Schlieve et al., 2017) and *CHAT* (cholinergic neurons) (Sang and Young, 1998), as well as the glial marker *S100B* (Young et al., 2003; Ferri et al., 1982) (Fig. 1B).

We next interrogated the cellular composition of our cultures using immunofluorescence. At D10 (one day after sphere plating under ENS-inducing conditions; Fig. 1A) cells started migrating out of the spheres and differentiating into neurons, which subsequently formed clustered, interconnected neuronal networks (Fig. S1A,B, Fig. 1C,D), in line with other differentiation protocols employing a similar sphere-formation step (Fattahi et al., 2016). By D22, PHOX2B protein was detected in the majority of peripherin-positive ($PRPH^+$) neurons in low-density regions (Fig. 1Ci) and, in a mutually exclusive manner with ASCL1, at the periphery of the re-plated spheres (Fig. 1Cii). In contrast, $ASCL1^+PHOX2B^-$ cells were largely confined to central regions within the spheres (Fig. 1C). These findings suggest a transition of ENS progenitors from an $ASCL1^+$ to a $PHOX2B^+PRPH^+$ pro-neural state as they migrate out of the dense three-dimensional sphere environment.

The presence of nitrergic and cholinergic neurons at both D22 and D50 was confirmed by expression of neuronal nitric oxide synthase (nNOS) and choline acetyltransferase (ChAT), alongside pan-neuronal ENS markers HUC/D and PGP9.5 (Krammer et al., 1993; Desmet et al., 2014) (Fig. 1D,E). At D50, cultures contained $PRPH^+PHOX2B^+$ clusters, occasionally including $ASCL1^+$ cells likely representing ENS progenitors committing to a neural fate (Fig. S1C). We also observed expression of the enteric neuron marker TRKC, while a subset of neurons exhibited immunoreactivity for tyrosine hydroxylase (TH), indicating a catecholaminergic character (Fig. S1D,E). A few cells expressed substance P, a neuropeptide found in subpopulations of excitatory neurons in the human ENS (Wattchow et al., 1988) (Fig. S1F). Finally, fibroblast-like cells were present in the cultures (as recently reported by Sabahi-Kaviani et al., 2026), potentially reflecting the mesenchymal potential of the vagal NC/ENS progenitors (Ling and Sauka-Spengler, 2019; Bixby et al., 2002) and/or possible contamination by cranial NC derivatives. We also investigated the induction of ENS progenitors and glial cells in our cultures. In the mouse embryo, early ENS progenitors co-express SOX10 and CD49d (ITGA4), which also mark their default glial character

Development (2026) 153, dev205775. doi:10.1242/dev.205775

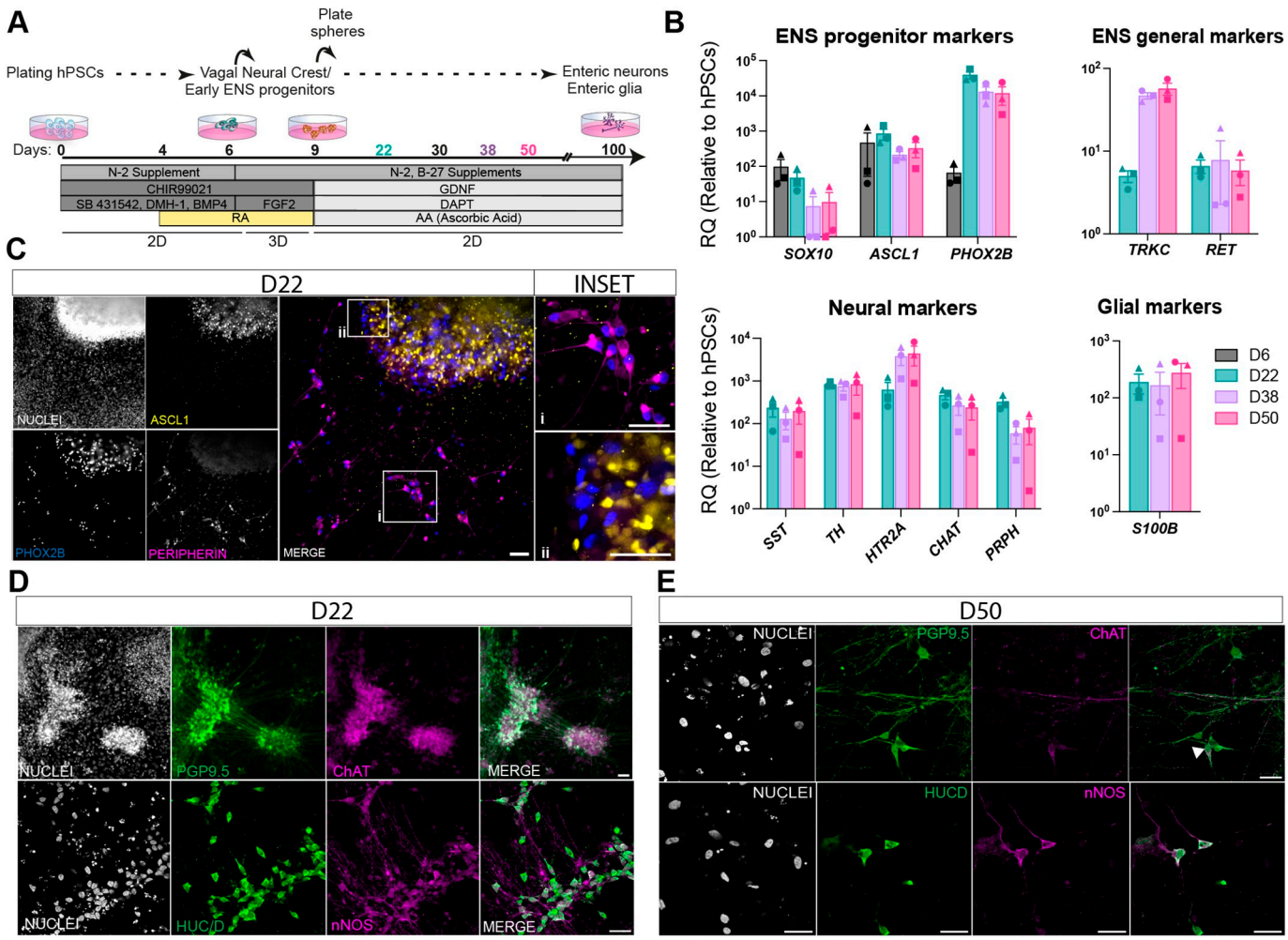


Fig. 1. *In vitro* generation of enteric neurons from hPSCs. (A) Schematic of the protocol showing time points and culture conditions used to generate ENS cultures from hPSCs *in vitro*, including both two-dimensional (2D) and three-dimensional (3D) steps. (B) qPCR-based gene expression analysis of ENS progenitor, neuronal and glial markers at the indicated time points. Data are mean±s.e.m., n=3 independent experiments with three replicates per experiment. D, differentiation day. (C) Immunofluorescence analysis of ASCL1, PHOX2B and peripherin expression in D22 hPSC-derived ENS cultures. Magnified regions of cells co-expressing peripherin and PHOX2B (i), and single ASCL1- and PHOX2B-positive cells (ii) are shown in the right-most panels (outlined in the lower magnification images). (D,E) Immunofluorescence analysis of the indicated enteric neuron markers in D22 (D) and D50 (E) cultures. Arrowhead in E indicates a neuronal cell body that is double-positive for PGP9.5 and ChAT. Scale bars: 50 µm in C; 30 µm in D,E.

acquired during later ENS development (Lasrado et al., 2017; Laddach et al., 2023). This transition toward a gliogenic state is accompanied by the upregulation of more-definitive glial markers such as S100β. Mapping of SOX10$^+$ and CD49d$^+$ cells using immunofluorescence analysis revealed that double-positive cells were already present at D11 (2 days after sphere plating) and persisted throughout the differentiation period examined up to D22 (Fig. 2A). Neuronal commitment, reflected by PGP9.5 expression, was apparent at D11 and coincided with the loss of CD49d expression, indicating exit from the progenitor state (Fig. 2B). At later differentiation stages (D22 and D50), SOX10$^+$CD49d$^+$ cells upregulated S100β expression, consistent with a transition to a glial fate; these glial cells were interspersed among TUJ1$^+$ neurons (Fig. 2C-E, Fig. S2C). Similar results were obtained using a second independent hPSC line: a WA09/H9 human embryonic stem cell (hESC)-derived SOX10:GFP line (Chambers et al., 2012) (Fig. S2). Together, these results demonstrate that our differentiation protocol successfully produces a diverse population of enteric neurons and glial cells from hPSCs.

Dynamics of Notch signalling component expression during the induction of human ENS cells

The final sphere-plating step of our protocol includes the addition of the Notch signalling/γ-secretase inhibitor DAPT (Fig. 1A), based on our observation that its inclusion significantly enhances the yield of ENS cells derived from hPSCs and consistent with previous reports on other neural differentiation protocols (Frith et al., 2020; Maury et al., 2015; Borghese et al., 2010). Given the established role of Notch signalling in mouse and zebrafish ENS development and its association with HSCR pathogenesis, we examined the effects of Notch inhibition in our human ENS differentiation model, comparing DAPT-treated cultures to DMSO-treated controls (Fig. 3A). To minimise potential off-target effects, we used the lowest effective concentration of DAPT (10 µM), which was sufficient to reduce the expression of canonical Notch target genes in hPSC-derived ENS cultures (Fig. S3A,B).

We first assayed the dynamics of Notch signalling component expression in our differentiating ENS cultures from D6 to D50 under control (DMSO) conditions using qPCR. We observed two

Development (2026) 153, dev205775. doi:10.1242/dev.205775

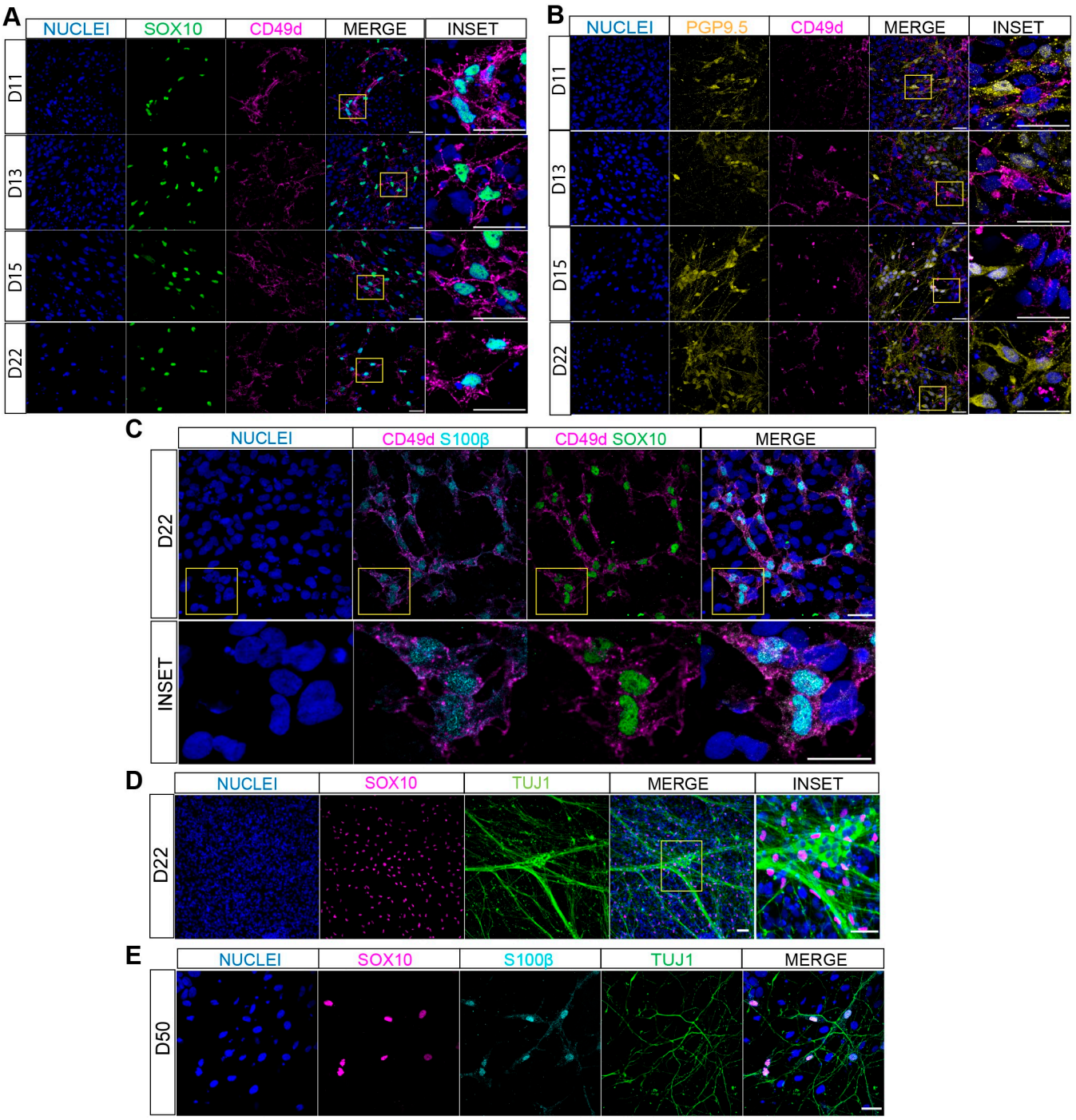


Fig. 2. *In vitro* generation of ENS progenitors and glia from hPSCs. (A,B) Immunofluorescence analysis of the expression of CD49d together with the ENS progenitor/glial marker SOX10 (A) or the neural marker PGP9.5 (B) at the indicated differentiation time points (D, days). Magnified areas are shown in the right-most panels (outlined in the lower magnification images). (C) Immunofluorescence analysis of the expression of CD49d together with the glial markers SOX10 and S100β in D22 cultures. Magnified regions of the indicated areas are shown in the lower panels (outlined in the top panels). (D,E) Immunofluorescence analysis of the expression of neuronal (TUJ1) and glial (SOX10 and S100β) markers in D22 (D) and D50 (E) cultures. Scale bars: 30 µm in A-C,E; 50 µm in D.

distinct expression patterns: high *NOTCH1*, *JAG1*, *DLL1*, *DLL3* and *DLL4* transcript levels were prevalent during the early phase of ENS differentiation (D13-22), suggesting a role in ENS progenitor cell fate decisions and early lineage commitment; in contrast, *NOTCH2* and *JAG2* expression increased during the later differentiation phase (D22-50), suggesting a role in committed enteric neurons and glia (Fig. 3B, DMSO control, black line). These findings are consistent with previous reports showing enrichment of *NOTCH1*, *DLL1* and *DLL3* transcripts in mouse ENS progenitors (Laddach et al., 2023; Morarach et al., 2021; Okamura and Saga, 2008). We also analysed the Notch target genes *HES1* and *HES5*. *HES5* expression peaked during the early progenitor-associated period, whereas *HES1* reached maximal levels at later differentiation stages (Fig. 3C, black line). DAPT

Development (2026) 153, dev205775. doi:10.1242/dev.205775

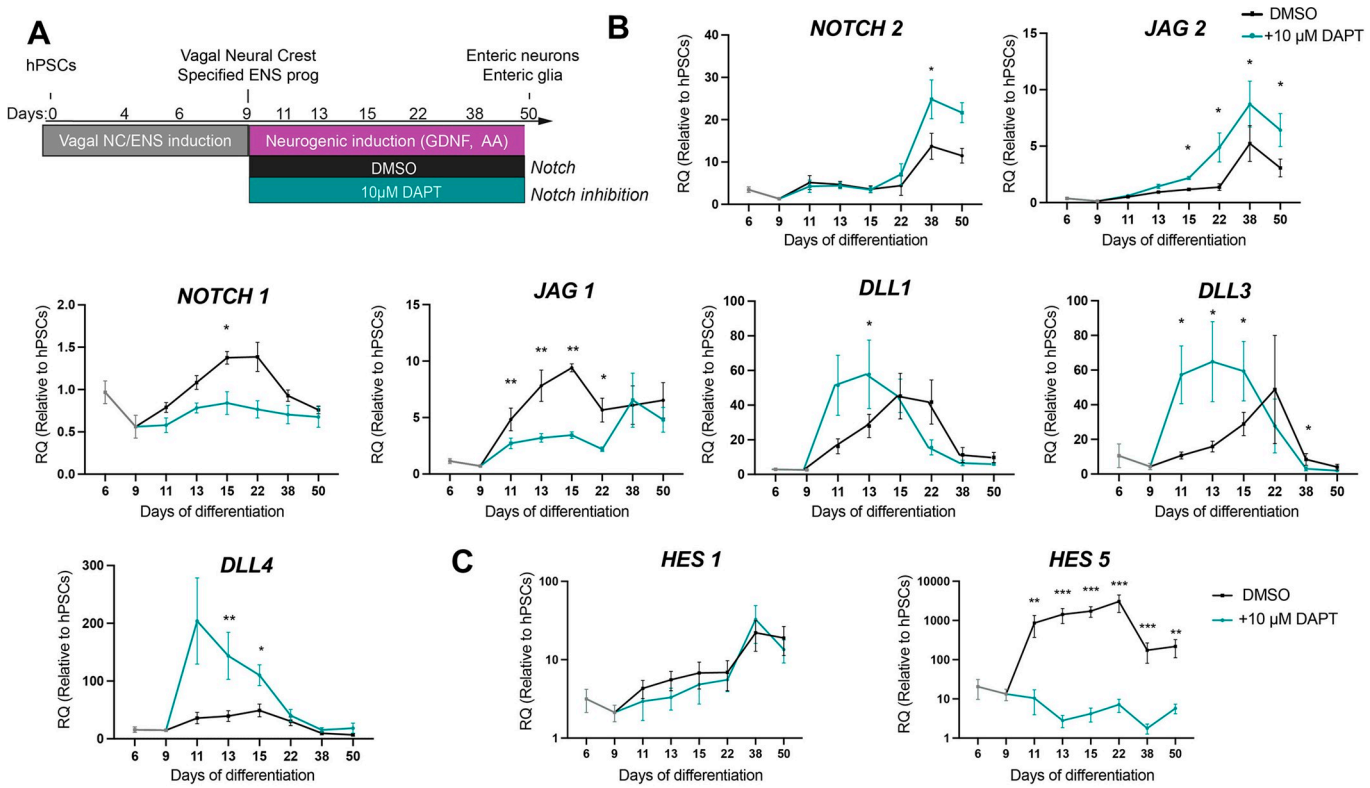


Fig. 3. Dynamics of Notch signalling component expression during human ENS differentiation. (A) Schematic of the time points and culture conditions used to generate ENS cultures with or without Notch pathway inhibition. (B) Time-course qPCR analysis of the indicated Notch signalling components in DMSO control (black line) and DAPT-treated (green line) ENS cultures. Data are mean±s.e.m., n=5 independent experiments with three replicates per experiment; *P<0.05, **P<0.01, ***P<0.001 [multiple paired two-tailed t-tests with Holm-Šídák correction for multiple comparisons (α = 0.05)]. Only statistically significant differences are indicated.

treatment markedly reduced *HES5* expression, confirming effective Notch pathway inhibition, while *HES1* levels were largely unaffected (Fig. 3C, green versus black lines). Furthermore, DAPT treatment significantly downregulated *NOTCH1* and *JAG1* (Fig. 3B), while triggering upregulation in *DLL1*, *DLL3* and *DLL4*, which also exhibited earlier expression peaks compared with DMSO controls (Fig. 3B). Collectively, these findings suggest that Notch signalling is active during hPSC-derived ENS cell specification and is regulated by the dynamic expression of distinct receptor and ligand-encoding genes, which exhibit differential temporal sensitivity to DAPT-mediated inhibition.

Notch signalling inhibition enhances human ENS progenitor differentiation

We next sought to define the impact of DAPT-mediated Notch signalling perturbation on ENS cell induction. Time-course qPCR analysis showed that DAPT treatment resulted in upregulation of both pro-neural-associated (*ASCL1*, *PHOX2B* and *PRPH*) and glial-associated (*SOX10* and *S100β*) transcripts at different time points throughout the course of differentiation (Fig. 4A,B). This was accompanied by an increase in the expression of enteric neuron subtype markers, such as *SST*, *TH* and *CHAT*, by D22 (Fig. S3C).

To further examine the effects of DAPT treatment on ENS progenitor dynamics, we assessed proteins marking ENS progenitor (SOX10$^+$S100β$^-$), neuronal (HUC/D, PERIPHERIN) and glial (SOX10$^+$S100β$^+$) identities at early (D15) and late (D22) differentiation stages. Under DMSO control conditions, the proportion of SOX10$^+$S100β$^+$ glial cells increased markedly from D15 to D22 (mean 64±15% in D22 versus 29±13% in D15, P<0.01) (Fig. 4C-E; dark-grey bars in Fig. 4E), possibly reflecting the default gliogenic fate of ENS progenitors, consistent with mouse studies (Laddach et al., 2023). In contrast, the production of HUC/D+ neurons remained relatively constant between these same two timepoints (Fig. 4F,G; dark grey bars in Fig. 4G).

Consistent with our previous observations (Frith et al., 2020), DAPT treatment significantly increased the percentage of HUC/D$^+$ cells compared with DMSO controls at both D15 (mean 34±15% in DAPT-treated versus 14±4% in control; P<0.05) and D22 (mean 45±23% in DAPT-treated versus 20±10% in control; P<0.05) (Fig. 4F,G). Additionally, DAPT treatment significantly increased the percentage of SOX10$^+$ cells at D15 and, to a lesser degree, at D22 (Fig. 4C,D). This expanded population consisted predominantly of SOX10$^+$S100β$^+$ glial cells (58±17% in DAPT versus 29±13% in control, P<0.01), with a corresponding reduction in SOX10$^+$S100β$^-$ ENS progenitors (Fig. 4C,E). As all S100β$^+$ enteric glial cells co-express SOX10, S100β single-positive cells, likely representing non-glial contaminants, were excluded from analysis (Hernandez-Ortega et al., 2024; Boesmans et al., 2015). The effect of DAPT on progenitor differentiation dynamics was also accompanied by enhanced neuronal clustering at D15, as revealed by nearest neighbour analysis showing a significantly reduced mean internuclear edge distance in DAPT-treated samples (Fig. 4H-J). Collectively, these data demonstrate that disruption of Notch signalling via the γ-secretase inhibitor DAPT enhances human ENS progenitor differentiation toward both neuronal and glial lineages.

Development (2026) 153, dev205775. doi:10.1242/dev.205775

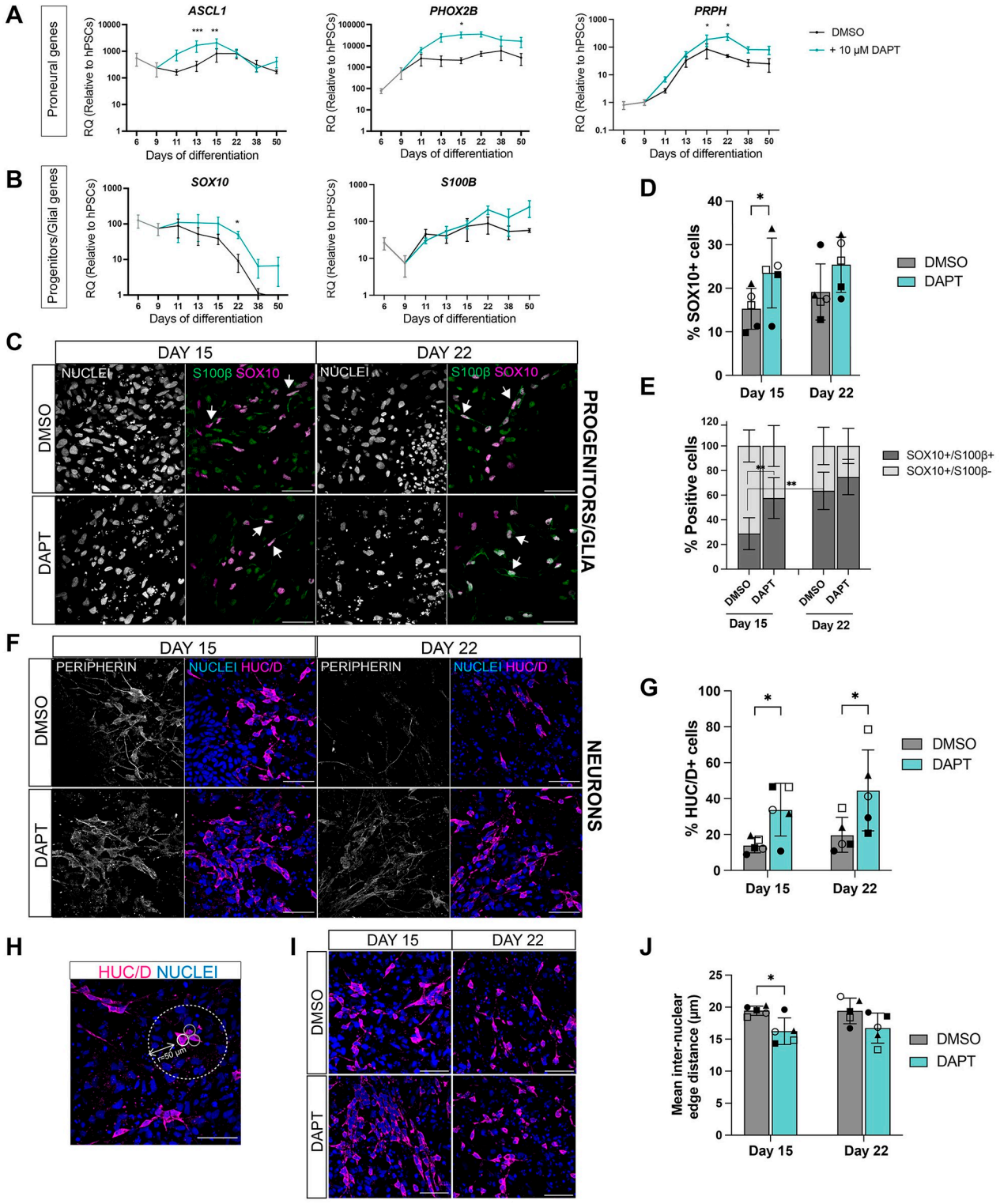


Fig. 4. See next page for legend.

Quantitative modelling supports a role for Notch signalling in regulating the pace of ENS progenitor differentiation

Extensive evidence from various developmental systems has indicated that Notch signalling is a key regulator of differentiation timing (Gonzalez and Reinberg, 2025; Bray and Bigas, 2025). We therefore employed a compartment modelling framework to evaluate how ENS progenitor differentiation rates and lineage biases evolve in our *in vitro* model, both with and without Notch inhibition (Fig. 5A-C). Using a compositional likelihood-based approach, we inferred parameter sets for which our simulations sufficiently match the empirical data (Fig. 4E,G). We tested four distinct scenarios: constant differentiation rate and lineage biases

Development (2026) 153, dev205775. doi:10.1242/dev.205775

Fig. 4. Notch signalling inhibition enhances human ENS progenitor differentiation. (A,B) Time-course qPCR analysis of the indicated proneural (A) and ENS progenitor/glial (B) genes in DMSO control (black line) and DAPT-treated (green line) cultures. Data are mean±s.e.m., n=5 independent experiments with three replicates per experiment. *P<0.05, **P<0.01, ***P<0.001 [multiple paired two-tailed t-tests with Holm-Šídák correction for multiple comparisons (α = 0.05)]. (C) Immunofluorescence analysis of SOX10 and S100β expression in control and DAPT-treated ENS cultures at days 15 and 22. Arrows indicate double-positive cells. (D) Quantification of the percentage of SOX10$^+$ cells per field of view at days 15 and 22. Data are mean±s.d., n=5 independent experiments, with 10-15 fields scored per condition, time point and experiment. Each biological replicate is represented by a unique symbol. *P<0.05 (two-tailed paired t-test). (E) Quantification of double-positive (SOX10$^+$S100 β$^+$; glia) and single-positive (SOX10$^+$S100$^-$; ENS progenitors) cells in control and DAPT-treated cultures at days 15 and 22. Stacked bars represent mean±s.d., n=5 independent experiments, with 15-30 fields scored per condition, time point and experiment; **P<0.01 (two-tailed paired t-test for the indicated comparisons). (F) Immunofluorescence analysis of peripherin and HUC/D expression in control and DAPT-treated ENS cultures at days 15 and 22. (G) Quantification of the percentage of HUC/D$^+$ cells per field of view at days 15 and 22. Data are mean±s.d., n=5 independent experiments, with 30 fields scored per condition and experiment for day 15, and 15 fields scored per condition and experiment for day 22. Each independent experiment is represented by a unique symbol. *P<0.05 (two-tailed paired t-test). (H) Method for measuring internuclear edge distances. Analysis was performed on all HUC/D$^+$ cells. As cytoplasmic boundaries were limited, nuclei were used as proxies to identify nearest neighbours. Using Delaunay triangulation, each nucleus (white outline) was paired with neighbouring nuclei (grey outline) within a 50 µm radius (white dotted line), and internuclear edge distances were calculated across the image. (I,J) Representative immunofluorescence images of HUC/D$^+$ cells (I) and quantification of mean internuclear edge distances (J) at days 15 and 22. Data are mean±s.d., n=5 independent experiments, each containing hundreds to thousands of HUC/D$^+$ cells. Each biological replicate is represented by a unique symbol; *P<0.05 (two-tailed paired t-test). Only statistically significant comparisons are indicated. Scale bars: 50 µm.

(CC); constant rate and time-varying biases (CV); time-varying rate and constant biases (VC); and time-varying rate and biases (VV). This approach aligns with that of Laddach et al. (2023), which identified a temporal neurogenic-to-gliogenic shift in the lineage bias of mouse ENS progenitors.

We first examined normal ENS progenitor differentiation using our SOX10, S100β and HUC/D expression data from D15 and D22 cultures. (Fig. 4E,G; DMSO). Simulated dynamics for the median posterior parameter values showed high fidelity to the observed data (Fig. 5D, Fig. S4A-D). 'Leave one biological replicate out' cross-validation did not identify a single preferred scenario, with differences in expected log predictive density between models small relative to their uncertainty (all within approximately two standard errors of the constant-rate, constant-bias model). This suggests that current experimental resolution is insufficient to definitively distinguish between these scenarios.

Analysis of inferred median posterior parameters across all models (Fig. S4E) showed comparable differentiation rates across scenarios (CC, 0.221 [0.102, 0.368]; VC, 0.226 [0.111, 0.397]; CV, 0.250 [0.113, 0.374]; VV, 0.242 [0.118, 0.403] day^{-1}; median and 95% credible interval), with all pairwise credible intervals overlapping across ≥94% of the narrower interval (Fig. 5E). In the time-varying models, the rate gradient was weakly identified, with credible intervals spanning zero (VC, −0.016 [−0.107, +0.016]; VV, −0.009 [−0.097, +0.015] day^{-2}) and posterior contraction relative to the prior of only 55% (for VC) and 64% (for VV) (Fig. 5F). At D22, the inferred differentiation rate was 0.000 day^{-1} [0.000, 0.424] (VC) and 0.103 day^{-1} [0.000, 0.441] (VV), computed per posterior draw as k^0+13k^1, and floored at zero, as in the forward model; the constant-rate models give 0.221 [0.102, 0.368] (CC) and 0.250 [0.113, 0.374] (CV) day^{-1} by construction. The breadth of these intervals reflects the weak identification of the gradient rather than evidence of a low terminal rate. In summary, the data do not resolve a temporal trend in differentiation rate over this interval. We therefore adopted the constant-rate models for subsequent analysis on the grounds of parsimony, noting that a declining rate is not excluded.

Regarding lineage biases, all models inferred a strong and consistent preference for the neuronal over the glial lineage (neuronal share of differentiation: CC, 0.741 [0.658, 0.811]; VC, 0.741 [0.660, 0.811]; CV, 0.894 [0.683, 0.993]; VV, 0.837 [0.608, 0.990]; median and 95% credible interval; Fig. 5G), reflecting previous reports of early neuronally biased ENS progenitors (Laddach et al., 2023). In the time-varying models, this neuronal share declined over time (CV, −0.033 [−0.063, +0.008] day^{-1}, posterior probability of a decline 0.95; VV, −0.029 [−0.084, +0.074] day^{-1}, probability 0.80; Fig. 5H), reaching 0.463 [0.141, 0.818] (CV) and 0.485 [0.000, 1.000] (VV) by D22, computed per posterior draw as $\rho^0+13\rho^1$. In the CV model, the decline is comparatively well resolved (86% posterior contraction relative to the prior) and carries the neuronal share across the 0.5 threshold, providing evidence for a time-dependent shift from neuronal towards glial production, consistent with previous work (Laddach et al., 2023); in the VV model, where the rate gradient is estimated simultaneously, it is not resolved. Within this timeframe, our data are nonetheless equally well described by a constant differentiation rate and a neuronally biased fate choice (Fig. 5I), which we adopted for subsequent analysis.

We next applied this framework to quantify kinetic shifts under Notch inhibition. As with the control, simulated dynamics (Fig. 5J, Fig. S5A-D) showed high fidelity to the data (Fig. 4E,G; DAPT), and again no single scenario was preferentially supported by cross-validation. Consistent trends emerged across the median posterior parameters (Fig. S5E). Notch inhibition increased the initial differentiation rate in all four models (CC, 0.415 [0.248, 0.514]; VC, 0.468 [0.257, 0.703]; CV, 0.408 [0.234, 0.511]; VV, 0.463 [0.266, 0.703] day^{-1}; median and 95% credible interval; Fig. 5K), with posterior probability of an increase relative to control exceeding 0.92 in every model and median estimates corresponding to an approximately twofold change (pooled ratio 1.84 [0.88, 4.27]), although the magnitude of the increase is imprecisely determined. In the time-varying models, the rate gradient was of similar magnitude to control (VC, −0.018 [−0.079, +0.010]; VV, −0.019 [−0.082, +0.010] day^{-2}; Fig. 5L), with credible intervals spanning zero and no detectable difference between conditions (VC, +0.001 [−0.067, +0.092]; VV, −0.007 [−0.072, +0.081] day^{-2}). Notch inhibition therefore elevates the differentiation rate without detectably altering its temporal trend over this interval.

In contrast to the differentiation rate, the neuronal versus glial bias was essentially unchanged under Notch inhibition: in the bias-constant models, the neuronal share of differentiation remained close to its control value (CC, 0.739 [0.648, 0.809] versus 0.741; VC, 0.743 [0.657, 0.810] versus 0.741; posterior probability of any between-condition difference 0.49 and 0.51, respectively; Fig. 5M), indicating that Notch inhibition accelerates differentiation without substantially altering the initial balance between neuronal and glial production. In the bias-varying models, however, the temporal trend differed in sign from control, the neuronal share increasing rather than declining over the interval

Development (2026) 153, dev205775. doi:10.1242/dev.205775

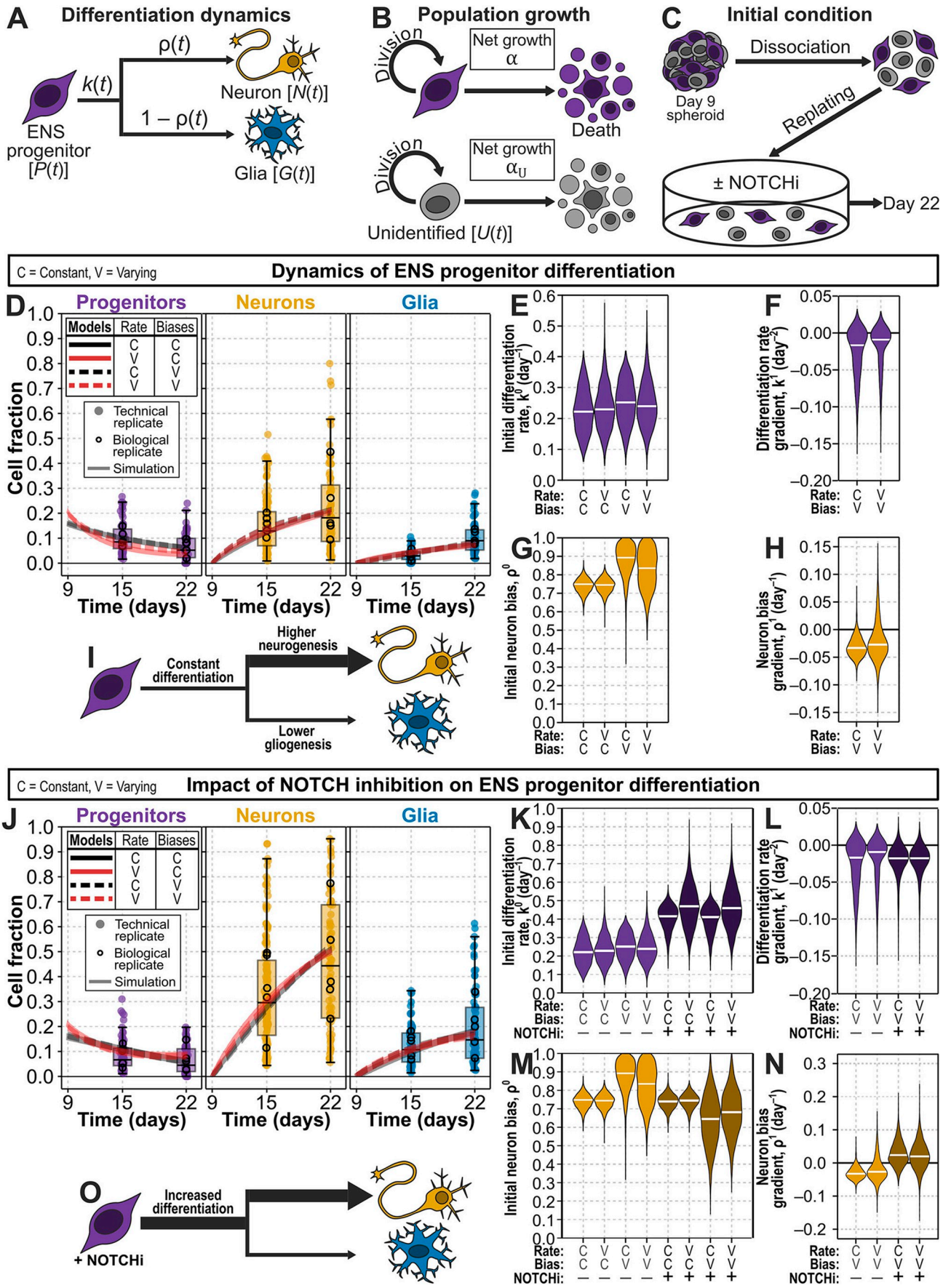


Fig. 5. See next page for legend.

Development (2026) 153, dev205775. doi:10.1242/dev.205775

Fig. 5. Quantitative modelling supports a role for Notch signalling in regulating the pace of human ENS progenitor differentiation. (A) Our modelling of ENS progenitor differentiation *in vitro* assumes that ENS progenitors, *P* (SOX10$^+$S100β$^-$), differentiate at per-capita rate *k* into neurons, *N* (HUC/D,), or glial cells, *G* (SOX10$^+$S100β$^+$), with neuronal and glial shares *ρ* and 1−*ρ*, respectively. (B) An unidentified population, *U* (SOX10$^-$S100β$^-$HUC/D$^-$), co-emerges in the cultures but is not derived from the ENS progenitors. ENS progenitors proliferate with net per-capita growth rate *α*, which takes into account both cell division and cell death; glia are produced by differentiation and do not appreciably self-renew; the unidentified population evolves with its own net per-capita rate α_U; and neurons are quiescent. (C) Initial conditions following dissociation and replating at day 9 of the differentiation protocol. (D) Numerical solutions using median posterior parameters from all four models (red and black solid and dashed lines) fitted to empirical data on ENS progenitor differentiation dynamics (markers and boxplots; see also Fig. 4E,G, DMSO). Filled circles indicate technical replicates and open circles indicate biological replicates. Box plots show the median (horizontal line); whiskers are Q1-1.5×IQR (bottom) and Q3 + 1.5×IQR (top), and are capped at the minimum or maximum technical replicate, respectively. (E-H) Posterior distributions of initial differentiation rates (E), differentiation rate gradients (F), initial lineage biases (G) and lineage bias gradients (H) for all four models. (I) Summary schematic of inferred ENS progenitor differentiation dynamics. (J) Numerical solutions using median posterior parameters from all four models (red and black solid and dashed lines) re-fitted to empirical data on ENS progenitor differentiation dynamics under NOTCH inhibition (markers and boxplots; see also Fig. 4E,G, DAPT). Filled circles indicate technical replicates, open circles indicate biological replicates, and box plots show the median and interquartile range (box) and Q1-1.5×IQR (whiskers) of technical replicate data. (K-N) Posterior distributions of initial differentiation rate (K), differentiation rate gradient (L), initial lineage bias (M) and neuronal lineage bias gradient (N) when re-fitted to NOTCH inhibition data. (O) Summary schematic for the inferred impact of NOTCH inhibition on ENS progenitor differentiation dynamics.

(CV, +0.024 [−0.034, +0.105]; VV, +0.020 [−0.052, +0.106] day^{-1}; Fig. 5N), reaching 0.948 [0.429, 1.000] (CV) and 0.935 [0.213, 1.000] (VV) by D22. The between-condition difference in this gradient was suggestive but not decisive (CV, +0.057 [−0.014, +0.143] day^{-1}, posterior probability 0.94; VV, +0.047 [−0.073, +0.150] day^{-1}, probability 0.82), and we therefore interpret it cautiously: the data are consistent with Notch inhibition sustaining, rather than progressively reducing, the neurogenic bias over this window. The pronounced between-condition shift in lineage bias reported previously was not supported once the unidentified cells were treated as a co-emerging population rather than a progenitor-derived fate.

Because the SOX10$^-$/S100β$^-$/HUC/D$^-$ co-emerging population is dynamically uncoupled from the ENS lineages in our model, the composition of the ENS compartment is independent of both α_U and P_0, and the parameter estimates and model comparison above are unaffected by how this population is treated. We therefore also present the data of Fig. 4E,G normalised to the ENS compartment alone (SOX10$^+$ progenitors, HUC/D$^+$ neurons and S100β$^+$ glia; Fig. S6). This presentation removes the effect of the declining unidentified fraction, which differs markedly between conditions (model-inferred median falling from 0.85 to 0.65 between D9 and D22 in control, and from 0.84 to 0.27 under Notch inhibition). Normalised in this way, the apparent increase in neuronal proportion in control between D15 and D22 (1.44-fold when expressed as a fraction of all cells) is largely attributable to this dilution effect, with the neuronal share of the ENS compartment essentially unchanged (0.54 to 0.53); the principal change within the compartment is a shift from progenitors to glia (0.35 to 0.20 and 0.12 to 0.27, respectively), consistent with the inferred lineage-bias dynamics. Corresponding values under Notch inhibition were 0.60 to 0.63 (neurons), 0.15 to 0.10 (progenitors) and 0.24 to 0.27 (glia).

This decline in the unidentified population is captured directly by its inferred net per-capita rate, which was indistinguishable from zero in control (α_U=−0.019 [−0.133, +0.079] day^{-1}) but negative under Notch inhibition (−0.121 [−0.241, −0.043] day^{-1}; posterior probability of a decline 1.00 in all four models), the between-condition difference being −0.103 [−0.254, +0.037] day^{-1} (posterior probability 0.92; Figs S4E and S5E). This population was the only one whose proportion decreased following Notch inhibition: comparing conditions at D22, the proportions of neurons and glia among all cells scored were higher under Notch inhibition (0.223 versus 0.456 and 0.102 versus 0.196, respectively; empirical biological-replicate means) and that of progenitors essentially unchanged (0.066 versus 0.067), whereas the progenitor share of the ENS compartment alone fell (0.195 versus 0.097; Fig. S6), consistent with accelerated differentiation.

Overall, Notch inhibition accelerates ENS progenitor differentiation increasing the production of both neurons and glia while leaving the neuronal versus glial bias largely stable, consistent with the branching model proposed recently (Laddach et al., 2023) in which an early neurogenic phase precedes a later gliogenic phase (Fig. 5O). These findings indicate that Notch signalling is a key regulator of the differentiation pace in ENS progenitors, ensuring the temporally refined production of neuronal and glial derivatives.

Notch-inhibited ENS progenitors exhibit impaired migration capacity

As ENS progenitor differentiation and migration are tightly coupled processes (Zhou et al., 2024; Uesaka et al., 2008; Baker et al., 2022; Young et al., 2004, 2014; McKeown et al., 2017), and considering that Notch inhibition induces both accelerated differentiation (Fig. 5) and HUC/D$^+$ neuron clustering at D15 (Fig. 4), we next investigated whether Notch signalling disruption also influences migratory behaviour. To this end, ENS cultures were treated with either DAPT or DMSO at the sphere-plating stage (D9), followed by a scratch assay at D14. Wound closure was then monitored over a 24 h period (up to D15) using live imaging (Fig. 6A).

DAPT treatment resulted in a delay in wound closure compared with DMSO-treated control ENS cultures (Fig. 6B,C, Fig. S7A,B). Immunostaining of scratch assay cultures at D15 revealed that wound closure in DMSO control cultures involved chain-like migration of SOX10$^+$ progenitors within the wound space and their association with nascent TUJ1$^{low/+}$ neuronal networks bridging the opposing wound sides (Fig. 6D). This may reflect the previously reported upregulation of neuronal markers in ENS progenitors during transition toward neural commitment (Zhou et al., 2024; Hao et al., 2009; Bondurand et al., 2006; Barlow et al., 2003). In contrast, DAPT treatment severely disrupted this process, evidenced by the absence of neuronal bridges and a reduction in the total number of cells and percentage of SOX10$^+$ ENS progenitors within the wound region (Fig. 6D-F). Further analysis of live-imaging data quantifying single-cell migration dynamics during wound closure showed that DAPT-treated ENS cultures exhibited reduced migration velocity and, most prominently, migration directionality compared with DMSO-treated controls (Fig. 6G, Fig. S7C). Together, these findings indicate that the intrinsic migratory behaviour of early ENS progenitors is influenced by Notch signalling and is likely linked to the timing of their differentiation toward neurons and glia.

Development (2026) 153, dev205775. doi:10.1242/dev.205775

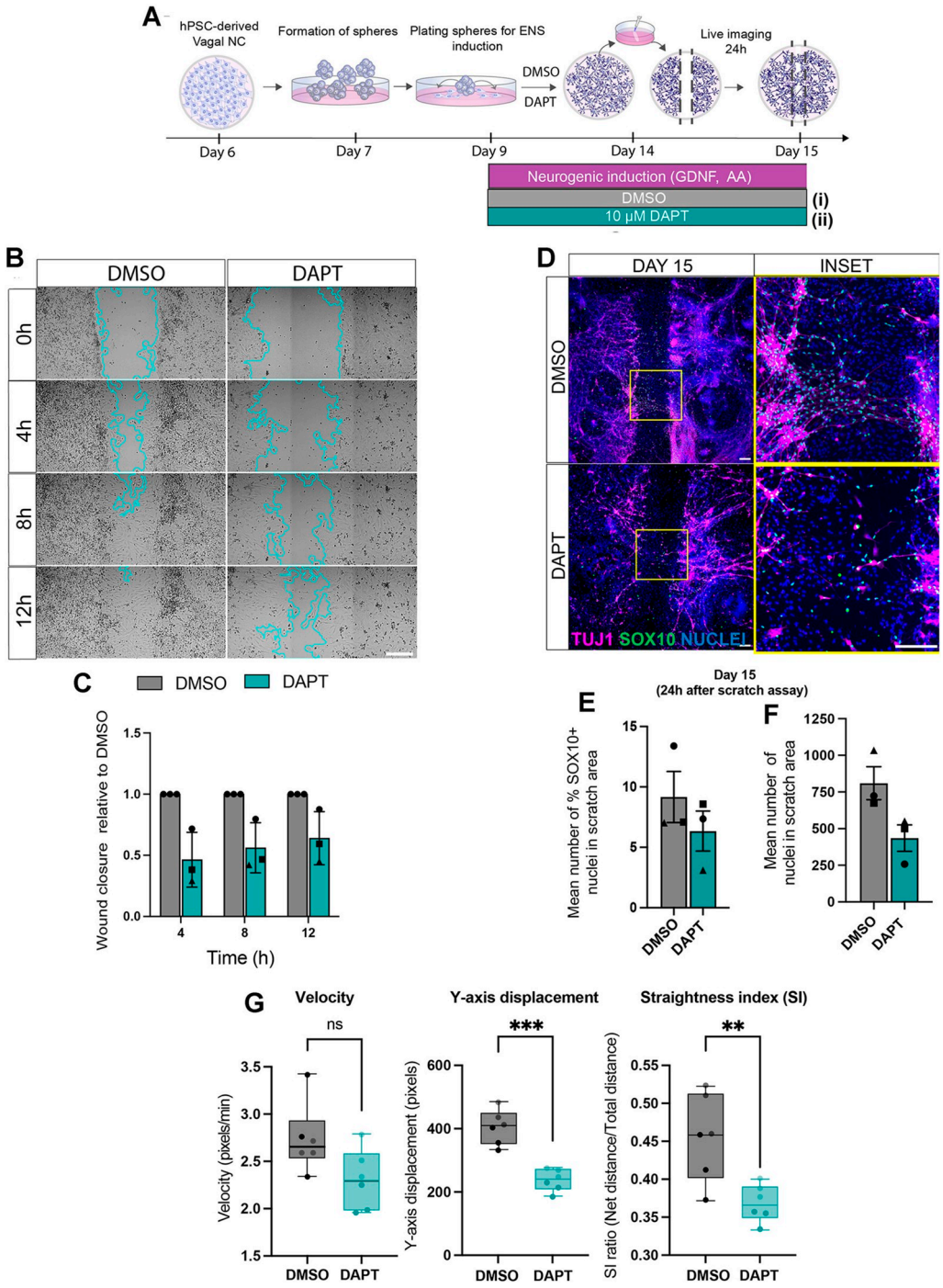


Fig. 6. Notch signalling inhibition impairs human ENS progenitor migration. (A) Schematic of the scratch assay. hPSC-derived vagal NC cells formed into spheres (day 6) and plated for ENS induction (day 9). By day 14, cells formed a confluent monolayer, after which a scratch was introduced using a pipette tip. Cell migration into the wound was monitored by live imaging. Notch pathway conditions were: (i) DMSO control added at day 9 (grey bars); and (ii) DAPT added at day 9 (green bars). (B) Time-lapse images of a representative scratch assay for DMSO- and DAPT-treated ENS cultures at 0, 4, 8 and 12 h post-scratch. Leading edges were detected using a segmentation algorithm (blue lines). Scale bar: 200 µm. (C) Wound closure relative to DMSO control (set as 1). Data are mean±s.d., *n*=3 independent experiments with 3-5 fields scored per condition. Fields were sampled from 1-3 wells per experiment. (D) Immunofluorescence analysis of SOX10 and TUJ1 in DMSO- and DAPT-treated ENS cultures at day 15 (24 h post-scratch). Areas outlined in the left panels are shown at higher magnification on the right. Scale bars: 200 µm. (E,F) Mean percentage of $SOX10^+$ cells and mean number of total nuclei in the wound area 24 h post-scratch. Data are mean±s.e.m., *n*=3 independent experiments with 4-10 fields scored per experiment. Each biological replicate is represented by a unique symbol. (G) Quantification of ENS cell migration parameters in the presence of DAPT/DMSO following live imaging of wound closure (see Fig. S7C): cell migration velocity (pixels/min) (left); *y*-axis displacement (pixels) representing directional migration toward the wound centre over time (centre); and straightness index (ratio of net displacement to total path length) measuring directional persistence during wound healing (right). Data are shown as box-and-whisker plots displaying the median (horizontal line), interquartile range (boxes) and minimum-to-maximum values (whiskers). Data points represent *n*=2 biological repeats per condition (light and dark points), 3 fields scored per condition and 10 cells per field. ***P<0.001, **P<0.01 (two-tailed unpaired *t*-test).

Development (2026) 153, dev205775. doi:10.1242/dev.205775

DISCUSSION

Several studies using animal models have revealed a multifaceted role for Notch signalling in controlling both ENS and NC development, encompassing progenitor maintenance, proliferation, migration and differentiation (Mead and Yutzey, 2012; Taylor et al., 2007; Okamura and Saga, 2008; Wakamatsu et al., 2000; Morrison et al., 2000; de Bellard et al., 2007; Delfino-Machin et al., 2017; Wiszniak and Schwarz, 2019; Okubo et al., 2021; Alhashem et al., 2022). These functions can be opposing, depending on developmental stage and specific ligand-receptor interactions. The importance of Notch is further highlighted by evidence that the expression of many of its components is perturbed in both animal models and individuals with HSCR, a potentially fatal enteric neuropathy resulting from lack of innervation of the distal bowel (Vincent et al., 2023; Li et al., 2023; Ngan et al., 2011; Windster et al., 2025; Tang et al., 2017; Jia et al., 2012). Despite this, the role of Notch signalling in human ENS progenitor ontogeny remains largely unexplored.

To address this, in this study we have characterised an *in vitro* model of human ENS development involving the stepwise differentiation of hPSCs into ENS progenitors, which subsequently give rise to enteric neurons (including multiple subtypes) and glia (Figs 1 and 2). To interrogate how the proportions of emerging enteric neurons and glia shift over time, we coupled our platform with computational modelling. Our results align with previous single-cell RNA-sequencing studies in mice, which suggest that early ENS progenitors are biased toward neurogenesis (Fig. 5) (Laddach et al., 2023). Crucially, this approach revealed that Notch signalling regulates the pace of ENS progenitor differentiation: DAPT-mediated inhibition led to a marked increase in both neuronal and glial numbers at the expense of the progenitor pool, driven by an accelerated rate of differentiation (Figs 4 and 5). This phenotype closely resembles that of mouse embryos lacking *Pofut1*, a core component of Notch signalling, in NC derivatives, where premature neuronal differentiation is accompanied by ENS progenitor depletion (Okamura and Saga, 2008). Although DAPT treatment appears to promote the generation of various enteric neuronal subtypes, including both cholinergic and nitrergic neurons (Fig. 1, Fig. S3C), it will be important to further determine whether Notch inhibition preferentially biases differentiation toward a specific neuronal differentiation trajectory, particularly given the reported expression of distinct Notch pathway components in later ENS populations (Morarach et al., 2021; Sander et al., 2003).

Similar observations have been reported in other neural progenitor systems (de la Pompa et al., 1997; Skeath and Carroll, 1992; Marklund et al., 2010; Trujillo-Paredes et al., 2016; Cheung et al., 2018), where Notch orchestrates differentiation timing to precursor pool size with the timely generation of derivatives. Interestingly, we found no evidence supporting the pro-gliogenic role of Notch signalling reported in the mouse ENS and peripheral nervous system (PNS) (Boesmans et al., 2021; Taylor et al., 2007; Mead and Yutzey, 2012; Okamura and Saga, 2008; Wakamatsu et al., 2000; Okubo et al., 2021; Wiszniak and Schwarz, 2019; Delfino-Machin et al., 2017). Instead, glial numbers appeared to increase following DAPT treatment, reflecting an accelerated overall rate of differentiation rather than a switch toward a gliogenic bias, as captured by our modelling, and suggesting species-specific differences or distinct temporal dynamics in human ENS development. It should be noted that our findings define the role of Notch signalling in the presence of GDNF, a key pro-ENS differentiation factor. Thus, investigating how Notch signalling interacts with extrinsic neurogenic cues to regulate human ENS development would be a key future research direction.

DAPT treatment also induced an earlier peak/potentiation in *DLL1*, *DLL3* and *DLL4* ligand expression, along with downregulation of *HES5* and *NOTCH1*, consistent with findings in *Notch1* and *RBP-Jk* mutant mice (de la Pompa et al., 1997). These results suggest that premature differentiation in our system may be mediated by a lateral inhibition feedback mechanism involving these Notch components, key fate determinants such as *SOX10* and *ASCL1*, and regulators of the cell cycle and other signalling pathways (e.g. Hedgehog and Wnt) (Okamura and Saga, 2008; Militi et al., 2023; Ngan et al., 2011). Given the dynamic temporal changes in the expression of Notch pathway components observed in the presence and absence of continuous DAPT treatment, a logical next step would be to define the stage-specific effects of Notch inhibition by targeting discrete windows of human ENS differentiation.

Our results further revealed that the accelerated generation of enteric neurons and glia in DAPT-treated cultures was accompanied by impaired migration of $SOX10^+$ ENS progenitors (Fig. 6). This was reflected by reduced migration velocity and directional persistence, indicating that Notch inhibition directly influences the intrinsic migratory behaviour of ENS progenitors, consistent with previous studies implicating Notch signalling in cardiac, vagal and trunk NC migration (Alhashem et al., 2022; Mead and Yutzey, 2012). An important avenue for future investigation will be to determine whether Notch signalling regulates collective ENS progenitor migration by coordinating cell–cell interactions and reciprocal proliferation status between leader and follower progenitors, as well as between ENS progenitors and neighbouring non-ENS cells, and how these interactions influence progenitor proliferation. Such a mechanism has been demonstrated in zebrafish trunk NC cells (Alhashem et al., 2022) and is further supported by single-cell transcriptomic analyses of wavefront ENS progenitors and their surrounding cells in the developing mouse embryo (Zhou et al., 2024).

Together, these findings support a model in which disruption of Notch signalling, either through direct mutation of pathway components (Ngan et al., 2011; Tang et al., 2017) or as a downstream consequence of attenuated ENS regulators (e.g. RET signalling; Vincent et al., 2023; Windster et al., 2025), can lead to aganglionic phenotypes. This occurs via premature differentiation from the ENS progenitor state and impaired progenitor migration – two key features of abnormal ENS development in HSCR.

MATERIALS AND METHODS

hPSC culture and differentiation

Human iPSCs (WTC11 and Rainbow WTC11; Miyaoka et al., 2014; El-Nachef et al., 2021) and H9 SOX10:GFP hESCs (Chambers et al., 2012) were routinely cultured in feeder-free conditions using Geltrex LDEV-Free reduced growth factor basement membrane matrix (A1413202, Thermo Fisher Scientific) and mTeSR medium (Stem Cell Technologies, 85850). Cells were passaged upon reaching approximately 80-90% confluency using PBS/EDTA (Invitrogen, 15575020) or ReleSR (Stem Cell Technologies, 05872).

Differentiation toward ENS cells was carried out as previously described (Gogolou et al., 2021). Briefly, hPSC cultures at 80-90% were dissociated into a single-cell suspension following treatment with Accutase (Merck Life Science, A6964) and plated at a density of 30-50,000 cells/cm^2 onto Geltrex-coated plates. Cells were cultured in DMEM/F12 (Merck, D6421) supplemented with 1× N2 (Thermo Fisher, 17502048), 1× non-essential amino acids (Thermo Fisher, 11140050), 1× Glutamax (Thermo Fisher, 35050061), CHIR99021 (1 µM; Tocris, 4423), SB431542 (2 µM; Tocris,

Development (2026) 153, dev205775. doi:10.1242/dev.205775

1614/1), BMP4 (20 ng/ml; Thermo Fisher, PHC9533) and DMH-1 (1 µM; Tocris, 4126/10) for 4 days. This was followed by the addition of all-trans retinoic acid (1 µM; Merck, R2625) for a further 2 days to generate vagal NC cells.

On D6, vagal NC cells were dissociated using Accutase and re-plated under non-adherent conditions to form free-floating spheres using Corning Ultra-Low attachment 6-well plates (Corning, 3471). Spheres were cultured for 3 days in medium containing 0.5x Neurobasal (Thermo Fisher, 21103049), 0.5× DMEM/F12 (Merck, D6421), 1× non-essential amino acids (Thermo Fisher, 11140050), 1× Glutamax (Thermo Fisher, 35050061), 1× N2 (Thermo Fisher, 17502048), 1× B27 (Thermo Fisher, 17504044), CHIR99021 (3 µM; Tocris, 4423), FGF2 (10 ng/ml; R&D Systems, 233-FB/CF), all-trans retinoic acid (1 µM; Merck, R2625) and Y-27632 2HCl (first 24 h; 10 µM; AdooQ Bioscience, A11001).

Finally, D9 spheres were collected and cultured for up to 50 days on Geltrex-coated plates in ENS-inducing medium containing 1× BrainPhys (StemCell Tech, 05790), 1× non-essential amino acids (Thermo Fisher, #11140050), 1× Glutamax (Thermo Fisher, 35050061), 1× N2 (Thermo Fisher, 17502048), 1× B27 (Thermo Fisher, 17504044), ascorbic acid (200 µM; Sigma-Aldrich, A8960) and GDNF (10 ng/ml; Peprotech, 450-10), in the presence of DAPT (10 µM dissolved in DMSO; Tocris, A2634) or an equivalent volume of DMSO alone (0.1% v/v) as vehicle control, as described in the Results section. ENS medium was changed every other day (half medium change).

For plating, D9 spheres were collected into a 50 ml conical tube and allowed to settle by gravity. Following careful removal of the medium, spheres from one well of the Ultra-Low attachment 6-well plate were resuspended and triturated in 4 ml of ENS induction medium, then plated at 1:4 and 1:8 dilutions in 12-well and 24-well plates, respectively.

For confocal microscopy, some wells of 12-well plates were fitted with 18 mm round glass coverslips (No. 1; VWR, MENZCB00180RAC20). These were pre-treated overnight at 37°C with poly-L-ornithine solution (50 µg/ml in PBS, Thermo Fisher, A31804) prior to Geltrex coating to facilitate adhesion.

To monitor migration of eGFP$^+$ progenitors from plated spheres, eGFP-WTC-11 cells – sorted and cloned from the WTC-11 rainbow reporter cell line containing a modified Brainbow cassette (El-Nachef et al., 2021) – were differentiated into vagal NC cells. On D6, these cells were mixed at a 1:10 ratio with stage-matched, unlabelled cells derived from the parental WTC-11 line and subjected to sphere formation for 3 days. Spheres were then re-plated under ENS-inducing conditions and live imaged for 75 h.

Quantitative real-time PCR

Total RNA was extracted using the Norgen total RNA purification kit (Norgen BioTek, 48200), following the manufacturer's instructions. Samples from undifferentiated hPSCs were collected as cell pellets immediately prior to initiating differentiation, representing the starting population used to generate the ENS cultures. RNA was extracted from these samples and analysed alongside the differentiated samples within the same qPCR experiment. cDNA synthesis was performed using the High-Capacity cDNA Reverse Transcription Kit (Thermo Fisher, 4368813), according to the manufacturer's instructions. Quantitative real-time PCR was carried out using the QuantStudio 12K Flex (Applied Biosystems) thermocycler in combination with the Roche Universal Probe Library system and TaqMan Fast Universal PCR Master Mix no AmpErase UNG (Applied Biosystems, 4366072). *GAPDH* was used as the housekeeping gene, serving as both a positive amplification control and reference gene for relative quantification normalization. Primer sequences (UPL probe number) were as follows: *GAPDH*, 5′-agccacatcgctcagacac-3′ and 5′-gcccaatacgaccaaatcc-3′ (#60); *SOX10*, 5′-ggctcccccatgtcagat-3′ and 5′-ctgtcttcggggtggttg-3′ (#21); *S100B*, 5′-gagctttcccatttcttagagga-3′ and 5′-gaagtcacattcgccgtctc-3′ (#47); *ASCL1*, 5′-cgacttcaccaactggttctg-3 and 5′-atgcaggttgtgcgatca-3′ (#38); *PHOX2B*, 5′-ctaccccgacatctacactcg-3′ and 5′-ctcctgcttgcgaaacttg-3′ (#17); *PRPH*, 5′-aagacgactgtgcctgaggt-3′ and 5′-tgctccttctgggactctgt-3′ (#10); *RET*, 5′-catcaggggtagcgaggtt-3′ and 5′-gggaaaggatgtgaaaaca-3′ (#17); *TRKC*, 5′-ccgtacgagagggtgacaat-3′ and 5′- tggtccagttcagattggtct-3′ (#21); *SST*, 5′-accccagactccgtcagttt-3′ and 5′-acagcagctctgccaagaag-3′ (#38); *CHAT*, 5′-cagccctgatgccttcat-3′ and 5′-cagtcttcgatggagcctgt-3′ (#78); *TH*, 5′-acgccaaggacaagctca-3′ and 5′-agcgtgtacgggtcgaact-3′ (#42); and *HTR2A*, 5′-tgatgtcacttgccatagctg-3′ and 5′-caggtaaatccagactgcacaa-3′ (#3). For Notch signalling-associated gene expression analysis, the following predesigned primer/probe mixtures (PrimeTime Gene Expression Assays, IDT) were used (assay IDs): *GAPDH*, Hs.PT.39a.22214836; *NOTCH1*, Hs.PT.58.23074795; *NOTCH2*, Hs.PT.58.28296019; *HES1*, Hs.PT.58.4181121; *HES5*, Hs.PT.58.14966721; *JAG1*, Hs.PT.56a.4972610; *JAG2*, Hs.PT.58.3493191; *DLL1*, Hs.PT.58.41063402; *DLL3*, Hs.PT.58.21516515; *DLL4*, Hs.PT.58.3416363. Graphs were generated using GraphPad Prism (GraphPad Software), which was also used for statistical analysis.

Immunofluorescence and image analysis

Cells were fixed in 4% paraformaldehyde (J61899.AP, VWR) for 10 min at room temperature. They were then permeabilised for 15 min at room temperature using 0.1-0.5% Triton X-100 in PBS (PBST), followed by incubation (1 h at room temperature or overnight at 4°C) in blocking buffer comprising 3% donkey serum (Jackson ImmunoResearch, 017-000-121) and 1% BSA in PBST. Primary and secondary antibodies, diluted in blocking buffer at the appropriate working concentrations (see below), were then added for 24-48 h at 4°C with gentle shaking on a rocking platform. Following primary antibody incubation, samples were washed at least three times for 5 min each with PBS, after which fluorophore-conjugated secondary antibody solution was added. Cells were incubated for 1-2 h at room temperature or overnight at 4°C in the dark. After secondary antibody incubation and nuclear counterstaining using Hoechst 33342 (Thermo Fisher Scientific, H3570), cells were washed three times with PBS prior to analysis. Fixed and stained cells on coverslips were mounted on 75×25 mm glass slides (VWR, Menzel Gläser, SuperFrost Plus) using VECTASHIELD mounting medium (2B Scientific, H-1700-10) and left to dry in the dark before imaging or storage at 4°C.

Fluorescent images were acquired using either the InCell Analyser 2200 system (GE Healthcare) or a LSM880 confocal system with Airyscan detectors (Zeiss). Images were first processed using ZEN (ZEISS) software, in the case of confocal imaging, and then analysed in Fiji (Schindelin et al., 2012). Identical brightness and contrast settings were applied across all images to enable comparison between different treatments. Samples incubated with secondary antibody solution only were used throughout to establish a threshold for positive signal, thereby minimising labelling artefacts introduced by fluorophore-conjugated secondary antibodies.

The following primary antibodies and dilutions were used: anti-SOX10 (1:500; CST, 89356); anti-SOX10 (1:200; R&D Systems, AF2864); anti-peripherin (1:60-1:100; Millipore Sigma, AB1530); anti-peripherin (1:200; Novus Biolog, NBP1-05423); anti-ASCL1 (1:100; Abcam, ab211327); anti-PGP9.5 (1:1000; Abcam, ab108986); anti-ChAT (1:200; Millipore Sigma, AB144P); anti-HuC/HuD (1:60-1:100; Invitrogen, A-21271); anti-PHOX2B (1:50; Santa Cruz, sc-376997); anti-S100 (β-subunit) (1:1000; Millipore Sigma, S2532); anti-S100 (1:50-1:250; Dako Omnis, Z0311); anti-beta III Tubulin(TuJ1) (1:1000; Abcam, ab78078); anti-beta III Tubulin(TuJ1) (1:1000; BioLegend, PRB-435P); anti-TRKC (1:500-1000; CST, 3376); anti-substance P (1:100; R&D Systems, MAB4375); anti-CD49d (1:1000; BioLegend, 304302); and anti-nNOS (1:400; Invitrogen #61-7000).

Protein expression was quantified using either: (1) CellProfiler (Carpenter et al., 2006) with custom pipelines for nuclear segmentation and intensity measurements; or (2) CellPose (Stringer et al., 2021) for nuclear segmentation using a custom-trained model, refined through iterative human-in-the-loop training, with segmentation masks imported into PickCells (https://pickcellslab.frama.io/docs/) for fluorescence intensity analysis. The latter approach was used to quantify HuC/D/SOX10/S100β-positive cells in ENS cultures.

Nearest-neighbour and internuclear edge distance analyses were performed using PickCells, as described previously (Punovuori et al., 2019). Cells were segmented using CellPose based on Hoechst 33342 nuclear staining, and segmentation masks were imported into PickCells. Nearest neighbours for each HUC/D$^+$ cell were identified using Delaunay triangulation. Given the limited cytoplasmic area, nuclei were used as proxies for cell positions. Distance between neighbouring cell membranes were calculated for each HUC/D$^+$ nucleus within a radius of 50 µm.

Development (2026) 153, dev205775. doi:10.1242/dev.205775

Scratch assay and wound closure analyses were performed on time-lapse data (see section below) using a previously published ImageJ plug-in (Suarez-Arnedo et al., 2020). The wound region at each time point was defined by a segmentation algorithm, and cell migration was quantified by measuring leading-edge progression over time. Percentage wound closure was calculated for each time point and condition relative to control (DMSO, set to 1). Scratch area was measured in μm^2. Statistical significance was calculated using GraphPad Prism (GraphPad Software).

Live imaging

Time-lapse microscopy was performed at 37°C and 5% CO_2 using either a Nikon Biostation CT or a Nikon Ti inverted microscope equipped with a stage-top incubation chamber and a DS-Fi3 colour camera. To monitor migration of $eGFP^+$ progenitors from plated spheres, the Nikon Biostation CT was used, with images captured every 10 min for 75 h using a 10× air objective. Images were acquired in both phase-contrast and green fluorescence channels. Image stacks were compiled in CL Quant (Nikon) and exported to Fiji (Schindelin et al., 2012) for analysis.

For scratch assay analysis, wound closure was imaged using either a Nikon Biostation CT or a Nikon Ti inverted microscope every 10 min for 24 h using a 10× air objective (either Plan Fluor Ph1 for phase contrast or Plan Apo λ for brightfield). Imaging positions were selected manually and 3-5 positions across 1-3 wells per condition and per experiment were monitored. Images were initially processed using Nikon software; where necessary, multiple fields of view were stitched to generate images spanning the full wound width, then exported to Fiji for analysis.

Scratch assay

D9 spheres were plated into Geltrex-coated 24-well plates in ENS induction medium (DMSO control or 10 µM DAPT or GDNF and Ascorbic Acid) and incubated at 37°C with 5% CO_2 until a confluent monolayer formed. On D14 of differentiation, a scratch assay was performed by manually removing cells from the centre of each well using a plastic 200 µl pipette tip. Wells were then washed three times with 1× PBS to remove detached cells, and fresh ENS medium containing either DMSO or 10 µM DAPT was added. Plates were incubated at 37°C and 5% CO_2 in either the Biostation CT or a stage-top incubation chamber on a Nikon Ti inverted microscope for 24 h, with images acquired every 10 min.

Quantification of cell migration dynamics

Single-cell migration dynamics were quantified using the Manual Tracking plugin in Fiji. Cell trajectories were analysed over a 6 h observation period starting from 3 h post-wounding. For each condition (DMSO/DAPT), 10 individual cells along the wound edge were manually traced per field of view (3 fields of view per condition). The experiment was conducted across 2 independent biological replicates, yielding a total of n=60 tracked cells per experimental group (30 cells per biological replicate). Spatial scale was maintained in pixel coordinates (1 pixel unit). To characterise cell movement, three key trajectory parameters were calculated from x, y coordinates across time: migration velocity, y-axis displacement and the straightness index (SI). Migration velocity, defined as the mean movement speed of each individual cell, was calculated over the entire tracking duration and subsequently averaged per field of view. Y-axis displacement, defined as the net spatial displacement along the y-axis (perpendicular to the initial wound edge), was measured to evaluate directional progress into the wound area. SI was quantified as the ratio of net direct displacement (D) to the total trajectory path length (L):

$$\mathrm{SI} = \frac{\mathrm{D}}{\mathrm{L}}.$$

A SI value approaching 1 indicates linear persistent migration, whereas values approaching 0 reflect random movement.

Mathematical modelling

We modelled the dynamics of ENS progenitor differentiation following the dissociation and replating of D9 neural spheroids and further culture for an additional 13 days, until D22 of differentiation, with (DAPT-treated) or without (DMSO control) NOTCH inhibition (NOTCHi) (Fig. 5C). Our mean-field model comprises a set of coupled ordinary differential equations (ODEs), which reflect our assumptions regarding cell-state transitions, proliferation and death (Fig. 5A,B). These equations govern the evolution in time (t) of the numbers of $SOX10^+/S100\beta^-/HUC/D^-$ progenitors (P), $SOX10^-/S100\beta^-/HUC/D^+$ neurons (N), $SOX10^+/S100\beta^+/HUC/D^-$ glia (G) and $SOX10^-/S100\beta^-/HUC/D^-$ unidentified cells (U).

We assumed that ENS progenitors differentiate irreversibly with per-capita rate $k(t)$ (Fig. 5A), giving rise to neurons and glia; the neuronal and glial shares of differentiation are set by a bias $\rho(t)$ and its complement $1-\rho(t)$, respectively. We assumed: that ENS progenitors proliferate with constant net per-capita rate α, which captures the net effect of division and death on cell number (Fig. 5B); that glia, given their low reported rate of division (Joseph et al., 2011; Laddach et al., 2023), do not appreciably self-renew; and that neurons are quiescent (Morarach et al., 2021). The $SOX10^-/S100\beta^-/HUC/D^-$ unidentified cells were treated as a co-emerging population that is not derived from the ENS progenitors but is present in the cultures, and evolves with its own net per-capita rate α_U. We assume the cells within the unidentified population represent mesenchymal-like cell types derived from day 6 vagal NC and/or cranial/cardiac NC contaminants.

Accounting for these processes led to the following ODE system describing cell population dynamics during differentiation with or without Notch inhibition:

$$\frac{dP}{dt} = -k(t)P + \alpha P, \tag{1}$$

$$\frac{dN}{dt} = k(t)\rho(t)P, \tag{2}$$

$$\frac{dG}{dt} = k(t)(1-\rho(t))P \text{ and} \tag{3}$$

$$\frac{dU}{dt} = \alpha_U U. \tag{4}$$

We assumed that immediately following replating at D9, no neurons or glia were present, so that $N(9) = 0$ and $G(9) = 0$. Furthermore, we assumed that an undetermined proportion (P_0) of cells at this time point were ENS progenitors, with the remainder unidentified. Finally, we scaled all dependent variables by the total cell number at D9, so that $P(9) = P_0$ and $U(9) = 1-P_0$. We assumed the same model structure with or without Notch inhibition.

We tested four distinct scenarios: constant differentiation rate and lineage biases (CC); constant rate and time-varying biases (CV); time-varying rate and constant biases (VC); and time-varying rate and biases (VV). The functional forms of k and ρ are given below:

Constant

$$k(t) = k^0 \text{ and} \tag{5}$$

$$\rho(t) = \rho^0, \quad i \in \{\mathrm{N}, \mathrm{G}\}. \tag{6}$$

Linear

$$k(t) = k^0 + k^1(t-9) \text{ and} \tag{7}$$

$$\rho(t) = \min\{\max\{\rho^0 + \rho^1 \ (t-9),\ 0\}, 1\} \tag{8}$$

The min/max expression in Eqn 8 ensures that the neuronal lineage bias does not fall below 0 or exceed 1.

Eqns 1-8 were solved numerically in Python; see the ‘Data and resource availability’ section for details on how to download our code.

Parameter inference and model selection

As most of our model parameters cannot be measured directly, they must be inferred from the data. Because our model predicts cell-type proportions rather than absolute numbers, and because the field-of-view counts are substantially over-dispersed relative to binomial sampling (varying

Development (2026) 153, dev205775. doi:10.1242/dev.205775

between biological replicates by considerably more than sampling alone would predict), we inferred parameters using a compositional likelihood evaluated directly on the observed counts, conditioning on the total number of cells counted in each field.

For each timepoint j and biological replicate r, let $\pi_P(t_j)$, $\pi_N(t_j)$, $\pi_G(t_j)$ and $\pi_U(t_j)$ denote the model-predicted proportions of progenitors, neurons, glia and unidentified cells, obtained by normalising the solution of Eqns 1-4 to the total cell number. In the neuronal field, the number of HUC/D$^+$ cells was modelled with a beta-binomial distribution:

$$y_{jr} \sim \text{BetaBinomial}(M^N_{jr}\varphi_N\pi_N(t_j), \varphi_N(1-\pi_N(t_j))),$$

where M^N_{jr} is the total number of cells scored in that field and y_{jr} the number that are HUC/D$^+$. In the SOX10/S100β field, the joint counts of SOX10$^+$S100β$^-$ progenitors (n_P), S100β$^+$ glia (n_G) and the remaining cells ($n_R = M^{PG}_{jr} - n_P - n_G$) were modelled with a Dirichlet-multinomial distribution:

$$(n_P, n_G,\ n_R)_{jr} \sim \text{DirichletMultinomial}(M^{PG}_{jr}, \varphi_{PG}(\pi_P(t_j), \pi_G(t_j), \pi_N(t_j) + \pi_U(t_j))),$$

where M^{PG}_{jr} is the total number of cells scored in that field and the remainder category corresponds to neurons and unidentified cells, which are not separately marked in this field. Here, φ_N and φ_{PG} are field-level concentration (precision) parameters that capture the between-replicate over-dispersion: larger values approach ordinary binomial or multinomial sampling, whereas smaller values admit greater replicate-to-replicate variability about the predicted proportions. Both were inferred jointly with the dynamical parameters. Since each distribution conditions on the observed field total, this likelihood compares predicted and observed proportions directly, and does not depend on the unknown initial cell number.

We sampled posterior distributions using the No-U-Turn sampler (Hoffman and Gelman, 2014), a self-tuning variant of Hamiltonian Monte Carlo implemented in NumPyro, running four independent chains per scenario. Weakly informative priors were placed on the time-varying rate and bias gradients to regularise the control condition, in which these gradients are only weakly identified. Convergence was assessed using the rank-normalised R-hat statistic and bulk and tail effective sample sizes (Vehtari et al., 2021); across all fitted parameters R-hat did not exceed 1.013, and we confirmed that an independent affine-invariant ensemble sampler (emcee; Foreman-Mackey et al., 2013) recovered indistinguishable posterior medians. The four scenarios were compared by ‘leave one biological replicate out’ cross-validation, quantified by the expected log predictive density (Vehtari et al., 2017), which evaluates each model’s ability to predict held-out experimental replicates rather than its in-sample fit. Parameter inference and model selection were performed using the experimental datasets shown in Fig. 4E,G, and we set parameter priors as shown in Table 1. The parameter P_0 was only inferred for −NOTCHi differentiation. This was then used for +NOTCH inference. A summary of inferred parameters can be found in Table S1.

Table 1. Parameter priors

Parameter	Constant	Time-varying
P_0	Uniform (0.1, 0.9)	Uniform(0.1, 0.9)
α	Uniform(−0.4, 0.4)	Uniform(−0.4, 0.4)
α_U	Uniform(−0.4, 0.4)	Uniform(−0.4, 0.4)
k^0	Uniform(0.01, 1.0)	Uniform(0.01, 1.0)
k^1	Normal(0, 0.05)	Normal(0, 0.05)
ρ^0	Uniform(0, 1)	Uniform(0, 1)
ρ^1	Normal(0, 0.05)	Normal(0, 0.05)
φ_N	logUniform(1, 2000)	logUniform(1, 2000)
φ_{PG}	logUniform(1, 2000)	logUniform(1, 2000)

Comparison of posterior parameter distributions

Between-condition differences in the inferred parameters were characterised by comparing their marginal posterior distributions directly, using the posterior medians and 90% credible intervals summarised in Table S1 and shown in Fig. 5E-H,K-N. We regarded a parameter as differing between the control and Notch-inhibited conditions when its marginal posteriors showed limited overlap, e.g. non-overlapping 90% credible intervals, and as essentially unchanged when the intervals overlapped substantially. We did not apply a formal significance test to the posterior samples, because with a large number of posterior draws such tests primarily reflect the precision with which each posterior is estimated rather than the magnitude of any biological difference.

Acknowledgements

We thank Darren Robinson and Nick Van Hateren for assistance with imaging, which was performed at the Wolfson Light Microscopy Facility, University of Sheffield, supported by a Biotechnology and Biological Sciences Research Council ALERT14 award (BB/M012522/1). We also thank Tom Frith, Chris Price and Rebecca Lea for technical support with the live-imaging experiments. Finally, we are grateful to Billy Douglas for his continuous support, and to Peter Andrews, Conor McCann and Celine Souilhol for critical reading of the manuscript.

Competing interests

The authors declare no competing or financial interests.

Author contributions

Conceptualization: A.T., A.G., N.S., S.E.S., A.G.F.; Data curation: A.G., N.S., F.C., S.E.S.; Formal analysis: A.G., N.S., F.C., S.E.S., A.G.F.; Funding acquisition: A.T., S.E.S., A.G.F.; Investigation: A.G., N.S., S.E.S., A.G.F.; Methodology: A.G., N.S., S.E.S., A.G.F.; Software: N.S., G.B., A.G.F.; Supervision: A.T., S.E.S., A.G.F.; Validation: A.G., N.S., S.E.S.; Visualization: A.G., N.S., S.E.S.; Writing – original draft: A.T., A.G., N.S., S.E.S., A.G.F.; Writing – review & editing: A.T., A.G., N.S., G.B., S.E.S., A.G.F.

Funding

This research was funded in part by the UKRI Medical Research Council (MR/V002163/1 and MR/Y013476/1 to A.T.), the European Union Horizon 2020 Framework Programme (H2020-EU.1.2.2; project 824070; A.T., and A.G.), the UKRI Biotechnology and Biological Sciences Research Council (White Rose Mechanistic Biology DTP studentship to N.S.), the Wellcome Trust (Sir Henry Wellcome Postdoctoral Fellowship 224070/Z/21/Z to S.E.S.) and the University of Sheffield (Strategic Research Fellowship in the Physics of Life and Quantitative Biology to S.E.S.). Open Access funding provided by the University of Sheffield. Deposited in PMC for immediate release.

Data and resource availability

All code used for simulations, model fitting and statistical analysis, together with datasets used for modelling, are publicly available on GitHub (https://github.com/AlexFletcher/gogolou_2026_notch). All other relevant data and details of resources can be found within the article and its supplementary information.

Peer review history

The peer review history is available online at https://journals.biologists.com/dev/lookup/doi/10.1242/dev.205775.reviewer-comments.pdf

References

Alhashem, Z., Feldner-Busztin, D., Revell, C., Alvarez-Garcillan Portillo, M., Camargo-Sosa, K., Richardson, J., Rocha, M., Gauert, A., Corbeaux, T., Milanetto, M. et al. (2022). Notch controls the cell cycle to define leader versus follower identities during collective cell migration. *eLife* **11**, e73550. doi:10.7554/eLife.73550

Baker, P. A., Ibarra-Garcia-Padilla, R., Venkatesh, A., Singleton, E. W. and Uribe, R. A. (2022). In toto imaging of early enteric nervous system development reveals that gut colonization is tied to proliferation downstream of Ret. *Development* **149**, dev200668. doi:10.1242/dev.200668

Barlow, A., DE Graaff, E. and Pachnis, V. (2003). Enteric nervous system progenitors are coordinately controlled by the G protein-coupled receptor EDNRB and the receptor tyrosine kinase RET. *Neuron* **40**, 905-916. doi:10.1016/S0896-6273(03)00730-X

Bixby, S., Kruger, G. M., Mosher, J. T., Joseph, N. M. and Morrison, S. J. (2002). Cell-intrinsic differences between stem cells from different regions of the peripheral nervous system regulate the generation of neural diversity. *Neuron* **35**, 643-656. doi:10.1016/S0896-6273(02)00825-5

Boesmans, W., Lasrado, R., Vanden Berghe, P. and Pachnis, V. (2015). Heterogeneity and phenotypic plasticity of glial cells in the mammalian enteric nervous system. *Glia* **63**, 229-241. doi:10.1002/glia.22746

Boesmans, W., Nash, A., Tasnády, K. R., Yang, W., Stamp, L. A. and Hao, M. M. (2021). Development, diversity, and neurogenic capacity of enteric glia. *Front. Cell Dev. Biol.* **9**, 775102. doi:10.3389/fcell.2021.775102

Bondurand, N., Natarajan, D., Barlow, A., Thapar, N. and Pachnis, V. (2006). Maintenance of mammalian enteric nervous system progenitors by SOX10 and endothelin 3 signalling. *Development* **133**, 2075-2086. doi:10.1242/dev.02375

Borghese, L., Dolezalova, D., Opitz, T., Haupt, S., Leinhaas, A., Steinfarz, B., Koch, P., Edenhofer, F., Hampl, A. and Brüstle, O. (2010). Inhibition of notch signaling in human embryonic stem cell-derived neural stem cells delays G1/S phase transition and accelerates neuronal differentiation in vitro and in vivo. *Stem Cells* **28**, 955-964. doi:10.1002/stem.408

Bray, S. J. (2016). Notch signalling in context. *Nat. Rev. Mol. Cell Biol.* **17**, 722-735. doi:10.1038/nrm.2016.94

Bray, S. J. and Bigas, A. (2025). Modes of Notch signalling in development and disease. *Nat. Rev. Mol. Cell Biol.* **26**, 522-537. doi:10.1038/s41580-025-00835-2

Carpenter, A. E., Jones, T. R., Lamprecht, M. R., Clarke, C., Kang, I. H., Friman, O., Guertin, D. A., Chang, J. H., Lindquist, R. A., Moffat, J. et al. (2006). CellProfiler: image analysis software for identifying and quantifying cell phenotypes. *Genome Biol.* **7**, R100. doi:10.1186/gb-2006-7-10-r100

Chalazonitis, A., Pham, T. D., Rothman, T. P., Distefano, P. S., Bothwell, M., Blair-Flynn, J., Tessarollo, L. and Gershon, M. D. (2001). Neurotrophin-3 is required for the survival-differentiation of subsets of developing enteric neurons. *J. Neurosci.* **21**, 5620-5636. doi:10.1523/JNEUROSCI.21-15-05620.2001

Chambers, S. M., Qi, Y., Mica, Y., Lee, G., Zhang, X. J., Niu, L., Bilsland, J., Cao, L., Stevens, E., Whiting, P. et al. (2012). Combined small-molecule inhibition accelerates developmental timing and converts human pluripotent stem cells into nociceptors. *Nat. Biotechnol.* **30**, 715-720. doi:10.1038/nbt.2249

Cheung, L., Le Tissier, P., Goldsmith, S. G., Treier, M., Lovell-Badge, R. and Rizzoti, K. (2018). NOTCH activity differentially affects alternative cell fate acquisition and maintenance. *eLife* **7**, e33318. doi:10.7554/eLife.33318

de Bellard, M. E., Ching, W., Gossler, A. and Bronner-Fraser, M. (2002). Disruption of segmental neural crest migration and ephrin expression in delta-1 null mice. *Dev. Biol.* **249**, 121-130. doi:10.1006/dbio.2002.0756

de Bellard, M. E., Barembaum, M., Arman, O. and Bronner-Fraser, M. (2007). Lunatic fringe causes expansion and increased neurogenesis of trunk neural tube and neural crest populations. *Neuron Glia Biol.* **3**, 93-103. doi:10.1017/S1740925X07000683

de la Pompa, J. L., Wakeham, A., Correia, K. M., Samper, E., Brown, S., Aguilera, R. J., Nakano, T., Honjo, T., Mak, T. W., Rossant, J. et al. (1997). Conservation of the Notch signalling pathway in mammalian neurogenesis. *Development* **124**, 1139-1148. doi:10.1242/dev.124.6.1139

Delfino-Machin, M., Madelaine, R., Busolin, G., Nikaido, M., Colanesi, S., Camargo-Sosa, K., Law, E. W., Toppo, S., Blader, P., Tiso, N. et al. (2017). Sox10 contributes to the balance of fate choice in dorsal root ganglion progenitors. *PLoS ONE* **12**, e0172947. doi:10.1371/journal.pone.0172947

Desmet, A. S., Cirillo, C. and vanden Berghe, P. (2014). Distinct subcellular localization of the neuronal marker HuC/D reveals hypoxia-induced damage in enteric neurons. *Neurogastroenterol. Motil.* **26**, 1131-1143. doi:10.1111/nmo.12371

El-Nachef, D., Bugg, D., Beussman, K. M., Steczina, S., Martinson, A. M., Murry, C. E., Sniadecki, N. J. and Davis, J. (2021). Engrafted human induced pluripotent stem cell-derived cardiomyocytes undergo clonal expansion in vivo. *Circulation* **143**, 1635-1638. doi:10.1161/CIRCULATIONAHA.119.044974

Fattahi, F., Steinbeck, J. A., Kriks, S., Tchieu, J., Zimmer, B., Kishinevsky, S., Zeltner, N., Mica, Y., El-Nachef, W., Zhao, H. et al. (2016). Deriving human ENS lineages for cell therapy and drug discovery in Hirschsprung disease. *Nature* **531**, 105-109. doi:10.1038/nature16951

Ferri, G. L., Probert, L., Cocchia, D., Michetti, F., Marangos, P. J. and Polak, J. M. (1982). Evidence for the presence of S-100 protein in the glial component of the human enteric nervous system. *Nature* **297**, 409-410. doi:10.1038/297409a0

Foreman-Mackey, D., Hogg, D. W., Lang, D. and Goodman, J. (2013). emcee: the MCMC hammer. *Publ. Astron. Soc. Pac.* **125**, 306-312. doi:10.1086/670067

Frith, T. J. R., Gogolou, A., Hackland, J. O. S., Hewitt, Z. A., Moore, H. D., Barbaric, I., Thapar, N., Burns, A. J., Andrews, P. W., Tsakiridis, A. et al. (2020). Retinoic acid accelerates the specification of enteric neural progenitors from *in-vitro*-derived neural crest. *Stem Cell Rep.* **15**, 557-565. doi:10.1016/j.stemcr.2020.07.024

Gogolou, A., Frith, T. J. R. and Tsakiridis, A. (2021). Generating enteric nervous system progenitors from human pluripotent stem cells. *Curr. Protoc.* **1**, e137. doi:10.1002/cpz1.137

Gonzalez, R. and Reinberg, D. (2025). The Notch pathway: a guardian of cell fate during neurogenesis. *Curr. Opin. Cell Biol.* **95**, 102543. doi:10.1016/j.ceb.2025.102543

Hao, M. M., Anderson, R. B., Kobayashi, K., Whitington, P. M. and Young, H. M. (2009). The migratory behavior of immature enteric neurons. *Dev. Neurobiol.* **69**, 22-35. doi:10.1002/dneu.20683

Hernandez-Ortega, K., Canul-Euan, A. A., Solis-Paredes, J. M., Borboa-Olivares, H., Reyes-Muñoz, E., Estrada-Gutierrez, G. and Camacho-Arroyo, I. (2024). S100B actions on glial and neuronal cells in the developing brain: an overview. *Front. Neurosci.* **18**, 1425525. doi:10.3389/fnins.2024.1425525

Heuckeroth, R. O. (2018). Hirschsprung disease - integrating basic science and clinical medicine to improve outcomes. *Nat. Rev. Gastroenterol. Hepatol.* **15**, 152-167. doi:10.1038/nrgastro.2017.149

Hoffman, M. D. and Gelman, A. (2014). The no-u-turn sampler: adaptively setting path lengths in Hamiltonian Monte Carlo. *J. Mach. Learn. Res.* **15**, 1593-1623.

Jacobs-Li, J., Tang, W., Li, C. and Bronner, M. E. (2023). Single-cell profiling coupled with lineage analysis reveals vagal and sacral neural crest contributions to the developing enteric nervous system. *eLife* **12**, e79156. doi:10.7554/eLife.79156

Jevans, B., Cooper, F., Fatieieva, Y., Gogolou, A., Kang, Y. N., Restuadi, R., Moulding, D., Vanden Berghe, P., Adameyko, I., Thapar, N. et al. (2024). Human enteric nervous system progenitor transplantation improves functional responses in Hirschsprung disease patient-derived tissue. *Gut* **73**, 1441-1453. doi:10.1136/gutjnl-2023-331532

Jia, H., Zhang, K., Chen, Q., Gao, H. and Wang, W. (2012). Downregulation of Notch-1/Jagged-2 in human colon tissues from Hirschsprung disease patients. *Int. J. Colorectal Dis.* **27**, 37-41. doi:10.1007/s00384-011-1295-4

Joseph, N. M., He, S., Quintana, E., Kim, Y. G., Núñez, G. and Morrison, S. J. (2011). Enteric glia are multipotent in culture but primarily form glia in the adult rodent gut. *J. Clin. Invest.* **121**, 3398-3411. doi:10.1172/JCI58186

Kang, Y. N., Fung, C. and vanden Berghe, P. (2021). Gut innervation and enteric nervous system development: a spatial, temporal and molecular tour de force. *Development* **148**, dev182543. doi:10.1242/dev.182543

Krammer, H. J., Karahan, S. T., Rumpel, E., Klinger, M. and Kühnel, W. (1993). Immunohistochemical visualization of the enteric nervous system using antibodies against protein gene product (PGP) 9.5. *Ann. Anat.* **175**, 321-325. doi:10.1016/S0940-9602(11)80029-4

Kuil, L. E., Kakiailatu, N. J. M., Windster, J. D., Bindels, E., Zink, J. T. M., van der Zee, G., Hofstra, R. M. W., Shepherd, I. T., Melotte, V. and Alves, M. M. (2023). Unbiased characterization of the larval zebrafish enteric nervous system at a single cell transcriptomic level. *iScience* **26**, 107070. doi:10.1016/j.isci.2023.107070

Laddach, A., Chng, S. H., Lasrado, R., Progatzky, F., Shapiro, M., Erickson, A., Sampedro Castaneda, M., Artemov, A. V., Bon-Frauches, A. C., Amaniti, E. M. et al. (2023). A branching model of lineage differentiation underpinning the neurogenic potential of enteric glia. *Nat. Commun.* **14**, 5904. doi:10.1038/s41467-023-41492-3

Lasrado, R., Boesmans, W., Kleinjung, J., Pin, C., Bell, D., Bhaw, L., McCallum, S., Zong, H., Luo, L., Clevers, H. et al. (2017). Lineage-dependent spatial and functional organization of the mammalian enteric nervous system. *Science* **356**, 722-726. doi:10.1126/science.aam7511

Le Douarin, N. M. and Teillet, M.-A. (1973). The migration of neural crest cells to the wall of the digestive tract in avian embryo. *J. Embryol. Exp. Morphol.* **30**, 31-48. doi:10.1242/dev.30.1.31

Li, Z., Lui, K. N., Lau, S. T., Lai, F. P., Li, P., Chung, P. H., Wong, K. K., Tam, P. K., Garica-Barcelo, M. M., Hui, C. C. et al. (2023). Transcriptomics of Hirschsprung disease patient-derived enteric neural crest cells reveals a role for oxidative phosphorylation. *Nat. Commun.* **14**, 2157. doi:10.1038/s41467-023-37928-5

Ling, I. T. C. and Sauka-Spengler, T. (2019). Early chromatin shaping predetermines multipotent vagal neural crest into neural, neuronal and mesenchymal lineages. *Nat. Cell Biol.* **21**, 1504-1517. doi:10.1038/s41556-019-0428-9

Liu, J. A. and Ngan, E. S. (2014). Hedgehog and Notch signaling in enteric nervous system development. *NeuroSignals* **22**, 1-13. doi:10.1159/000356305

Marklund, U., Hansson, E. M., Sundstrom, E., de Angelis, M. H., Przemeck, G. K., Lendahl, U., Muhr, J. and Ericson, J. (2010). Domain-specific control of neurogenesis achieved through patterned regulation of Notch ligand expression. *Development* **137**, 437-445. doi:10.1242/dev.036806

Maury, Y., Côme, J., Piskorowski, R. A., Salah-Mohellibi, N., Chevaleyre, V., Peschanski, M., Martinat, C. and Nedelec, S. (2015). Combinatorial analysis of developmental cues efficiently converts human pluripotent stem cells into multiple neuronal subtypes. *Nat. Biotechnol.* **33**, 89-96. doi:10.1038/nbt.3049

McCallum, S., Obata, Y., Fourli, E., Boeing, S., Peddie, C. J., Xu, Q., Horswell, S., Kelsh, R. N., Collinson, L., Wilkinson, D. et al. (2020). Enteric glia as a source of neural progenitors in adult zebrafish. *eLife* **9**, e56086. doi:10.7554/eLife.56086

McKeown, S. J., Mohsenipour, M., Bergner, A. J., Young, H. M. and Stamp, L. A. (2017). Exposure to GDNF enhances the ability of enteric neural progenitors to generate an enteric nervous system. *Stem Cell Rep.* **8**, 476-488. doi:10.1016/j.stemcr.2016.12.013

Mead, T. J. and Yutzey, K. E. (2012). Notch pathway regulation of neural crest cell development in vivo. *Dev. Dyn.* **241**, 376-389. doi:10.1002/dvdy.23717

Memic, F., Knoflach, V., Sadler, R., Tegerstedt, G., Sundström, E., Guillemot, F., Pachnis, V. and Marklund, U. (2016). Ascl1 is required for the development of specific neuronal subtypes in the enteric nervous system. *J. Neurosci.* **36**, 4339-4350. doi:10.1523/JNEUROSCI.0202-16.2016

Militi, S., Nibhani, R., Jalali, M. and Pauklin, S. (2023). RBL2-E2F-GCN5 guide cell fate decisions during tissue specification by regulating cell-cycle-dependent fluctuations of non-cell-autonomous signaling. *Cell Rep.* **42**, 113146. doi:10.1016/j.celrep.2023.113146

Miyaoka, Y., Chan, A. H., Judge, L. M., Yoo, J., Huang, M., Nguyen, T. D., Lizarraga, P. P., So, P. L. and Conklin, B. R. (2014). Isolation of single-base genome-edited human iPS cells without antibiotic selection. *Nat. Methods* **11**, 291-293. doi:10.1038/nmeth.2840

Morarach, K., Mikhailova, A., Knoflach, V., Memic, F., Kumar, R., Li, W., Ernfors, P. and Marklund, U. (2021). Diversification of molecularly defined myenteric neuron classes revealed by single-cell RNA sequencing. *Nat. Neurosci.* **24**, 34-46. doi:10.1038/s41593-020-00736-x

Morrison, S. J., Perez, S. E., Qiao, Z., Verdi, J. M., Hicks, C., Weinmaster, G. and Anderson, D. J. (2000). Transient Notch activation initiates an irreversible switch from neurogenesis to gliogenesis by neural crest stem cells. *Cell* **101**, 499-510. doi:10.1016/S0092-8674(00)80860-0

Ngan, E. S., Garcia-Barceló, M. M., Yip, B. H., Poon, H. C., Lau, S. T., Kwok, C. K., Sat, E., Sham, M. H., Wong, K. K., Wainwright, B. J. et al. (2011). Hedgehog/Notch-induced premature gliogenesis represents a new disease mechanism for Hirschsprung disease in mice and humans. *J. Clin. Invest.* **121**, 3467-3478. doi:10.1172/JCI43737

Okamura, Y. and Saga, Y. (2008). Notch signaling is required for the maintenance of enteric neural crest progenitors. *Development* **135**, 3555-3565. doi:10.1242/dev.022319

Okubo, Y., Ohtake, F., Igarashi, K., Yasuhiko, Y., Hirabayashi, Y., Saga, Y. and Kanno, J. (2021). Cleaved Delta like 1 intracellular domain regulates neural development via Notch signal-dependent and -independent pathways. *Development* **148**, dev193664. doi:10.1242/dev.193664

Pattyn, A., Morin, X., Cremer, H., Goridis, C. and Brunet, J. F. (1999). The homeobox gene Phox2b is essential for the development of autonomic neural crest derivatives. *Nature* **399**, 366-370. doi:10.1038/20700

Punovuori, K., Migueles, R. P., Malaguti, M., Blin, G., MacLeod, K. G., Carragher, N. O., Pieters, T., van Roy, F., Stemmler, M. P. and Lowell, S. (2019). N-cadherin stabilises neural identity by dampening anti-neural signals. *Development* **146**, dev183269. doi:10.1242/dev.183269

Recinto, S. J., Premachandran, S., Mukherjee, S., Allot, A., MacDonald, A., Yaqubi, M., Gruenheid, S., Trudeau, L. E. and Stratton, J. A. (2024). Characterizing enteric neurons in dopamine transporter (DAT)-Cre reporter mice reveals dopaminergic subtypes with dual-transmitter content. *Eur. J. Neurosci.* **59**, 2465-2482. doi:10.1111/ejn.16307

Sabahi-Kaviani, R., Gogolou, A., Souilhol, C., van der Kroeg, M., Kushner, S. A., de Vrij, F. M. S., Tsakiridis, A. and Luttge, R. (2026). Nervous system-on-chip: innovative microfluidic platform to compartmentalize hiPSC-derived neural networks. *Micromachines (Basel)* **17**, 199. doi:10.3390/mi17020199

Sander, G. R., Brookes, S. J. and Powell, B. C. (2003). Expression of Notch1 and Jagged2 in the enteric nervous system. *J. Histochem. Cytochem.* **51**, 969-972. doi:10.1177/002215540305100712

Sang, Q. and Young, H. M. (1998). The identification and chemical coding of cholinergic neurons in the small and large intestine of the mouse. *Anat. Rec.* **251**, 185-199. doi:10.1002/(SICI)1097-0185(199806)251:2<185::AID-AR6>3.0.CO;2-Y

Schindelin, J., Arganda-Carreras, I., Frise, E., Kaynig, V., Longair, M., Pietzsch, T., Preibisch, S., Rueden, C., Saalfeld, S., Schmid, B. et al. (2012). Fiji: an open-source platform for biological-image analysis. *Nat. Methods* **9**, 676-682. doi:10.1038/nmeth.2019

Schlieve, C. R., Fowler, K. L., Thornton, M., Huang, S., Hajjali, I., Hou, X., Grubbs, B., Spence, J. R. and Grikscheit, T. C. (2017). Neural crest cell implantation restores enteric nervous system function and alters the gastrointestinal transcriptome in human tissue-engineered small intestine. *Stem Cell Rep.* **9**, 883-896. doi:10.1016/j.stemcr.2017.07.017

Skeath, J. B. and Carroll, S. B. (1992). Regulation of proneural gene expression and cell fate during neuroblast segregation in the Drosophila embryo. *Development* **114**, 939-946. doi:10.1242/dev.114.4.939

Stringer, C., Wang, T., Michaelos, M. and Pachitariu, M. (2021). Cellpose: a generalist algorithm for cellular segmentation. *Nat. Methods* **18**, 100-106. doi:10.1038/s41592-020-01018-x

Suarez-Arnedo, A., Torres Figueroa, F., Clavijo, C., Arbelaez, P., Cruz, J. C. and Munoz-Camargo, C. (2020). An image J plugin for the high throughput image analysis of in vitro scratch wound healing assays. *PLoS ONE* **15**, e0232565. doi:10.1371/journal.pone.0232565

Szabolcs, M. J., Visser, J., Shelanski, M. L., O'toole, K. and Schullinger, J. N. (1996). Peripherin: a novel marker for the immunohistochemical study of malformations of the enteric nervous system. *Pediatr. Pathol. Lab. Med.* **16**, 51-70. doi:10.1080/15513819609168661

Tang, W., Tang, J., Zhao, Y., Qin, Y., Jin, G., Xu, X., Zhu, H., Shen, H., Wang, X., Hu, Z. et al. (2017). Exome-wide association study identified new risk loci for Hirschsprung's disease. *Mol. Neurobiol.* **54**, 1777-1785. doi:10.1007/s12035-016-9752-2

Taraviras, S., Marcos-Gutierrez, C. V., Durbec, P., Jani, H., Grigoriou, M., Sukumaran, M., Wang, L. C., Hynes, M., Raisman, G. and Pachnis, V. (1999). Signalling by the RET receptor tyrosine kinase and its role in the development of the mammalian enteric nervous system. *Development* **126**, 2785-2797. doi:10.1242/dev.126.12.2785

Taylor, M. K., Yeager, K. and Morrison, S. J. (2007). Physiological Notch signaling promotes gliogenesis in the developing peripheral and central nervous systems. *Development* **134**, 2435-2447. doi:10.1242/dev.005520

Trujillo-Paredes, N., Valencia, C., Guerrero-Flores, G., Arzate, D. M., Baizabal, J. M., Guerra-Crespo, M., Fuentes-Hernández, A., Zea-Armenta, I. and Covarrubias, L. (2016). Regulation of differentiation flux by Notch signalling influences the number of dopaminergic neurons in the adult brain. *Biol. Open* **5**, 336-347. doi:10.1242/bio.013383

Uesaka, T., Nagashimada, M., Yonemura, S. and Enomoto, H. (2008). Diminished Ret expression compromises neuronal survival in the colon and causes intestinal aganglionosis in mice. *J. Clin. Invest.* **118**, 1890-1898. doi:10.1172/JCI34425

Vehtari, A., Gelman, A. and Gabry, J. (2017). Practical Bayesian model evaluation using leave-one-out cross-validation and WAIC. *Stat. Comput.* **27**, 1413-1432. doi:10.1007/s11222-016-9696-4

Vehtari, A., Gelman, A., Simpson, D., Carpenter, B. and Bürkner, P.-C. (2021). Rank-Normalization, Folding, and Localization: An Improved R for Assessing Convergence of MCMC (with Discussion). *Bayesian Anal.* **16**, 667-718. doi:10.1214/20-BA1221

Vincent, E., Chatterjee, S., Cannon, G. H., Auer, D., Ross, H., Chakravarti, A. and Goff, L. A. (2023). Ret deficiency decreases neural crest progenitor proliferation and restricts fate potential during enteric nervous system development. *Proc. Natl. Acad. Sci. USA* **120**, e2211986120. doi:10.1073/pnas.2211986120

Wakamatsu, Y., Maynard, T. M. and Weston, J. A. (2000). Fate determination of neural crest cells by NOTCH-mediated lateral inhibition and asymmetrical cell division during gangliogenesis. *Development* **127**, 2811-2821. doi:10.1242/dev.127.13.2811

Wattchow, D. A., Furness, J. B. and Costa, M. (1988). Distribution and coexistence of peptides in nerve fibers of the external muscle of the human gastrointestinal tract. *Gastroenterology* **95**, 32-41. doi:10.1016/0016-5085(88)90287-9

Windster, J. D., Kakiailatu, N. J. M., Kuil, L. E., Antanaviciute, A., Sacchetti, A., MacKenzie, K. C., Peulen-Zink, J., Kan, T. W., Bindels, E., de Pater, E. et al. (2025). Human enteric glia diversity in health and disease: new avenues for the treatment of Hirschsprung disease. *Gastroenterology* **168**, 965-979.e12. doi:10.1053/j.gastro.2024.12.011

Wiszniak, S. and Schwarz, Q. (2019). Notch signalling defines dorsal root ganglia neuroglial fate choice during early neural crest cell migration. *BMC Neurosci.* **20**, 21. doi:10.1186/s12868-019-0501-0

Yntema, C. L. and Hammond, W. S. (1954). The origin of intrinsic ganglia of trunk viscera from vagal neural crest in the chick embryo. *J. Comp. Neurol.* **101**, 515-541. doi:10.1002/cne.901010212

Young, H. M., Bergner, A. J. and Müller, T. (2003). Acquisition of neuronal and glial markers by neural crest-derived cells in the mouse intestine. *J. Comp. Neurol.* **456**, 1-11. doi:10.1002/cne.10448

Young, H. M., Bergner, A. J., Anderson, R. B., Enomoto, H., Milbrandt, J., Newgreen, D. F. and Whitington, P. M. (2004). Dynamics of neural crest-derived cell migration in the embryonic mouse gut. *Dev. Biol.* **270**, 455-473. doi:10.1016/j.ydbio.2004.03.015

Young, H. M., Bergner, A. J., Simpson, M. J., McKeown, S. J., Hao, M. M., Anderson, C. R. and Enomoto, H. (2014). Colonizing while migrating: how do individual enteric neural crest cells behave? *BMC Biol.* **12**, 23. doi:10.1186/1741-7007-12-23

Zhang, D., Rollo, B. N., Nagy, N., Stamp, L. and Newgreen, D. F. (2019). The enteric neural crest progressively loses capacity to form enteric nervous system. *Dev. Biol.* **446**, 34-42. doi:10.1016/j.ydbio.2018.11.017

Zhou, B., Feng, C., Sun, S., Chen, X., Zhuansun, D., Wang, D., Yu, X., Meng, X., Xiao, J., Wu, L. et al. (2024). Identification of signaling pathways that specify a subset of migrating enteric neural crest cells at the wavefront in mouse embryos. *Dev. Cell* **59**, 1689-1706.e8. doi:10.1016/j.devcel.2024.03.034